AD-A189 237 LOW-FREQUENCY REVERBERATION MEASUREMENTS WITH AN ACTIVATED TOWED ARRAY: S..(U) SACLANT ASW RESEARCH CENTRE LA SPEZIA (ITALY) D MARANDINO OCT 87 1/1

UNCLASSIFIED SACLANTCEN-SR-112 F/G 17/1 NL

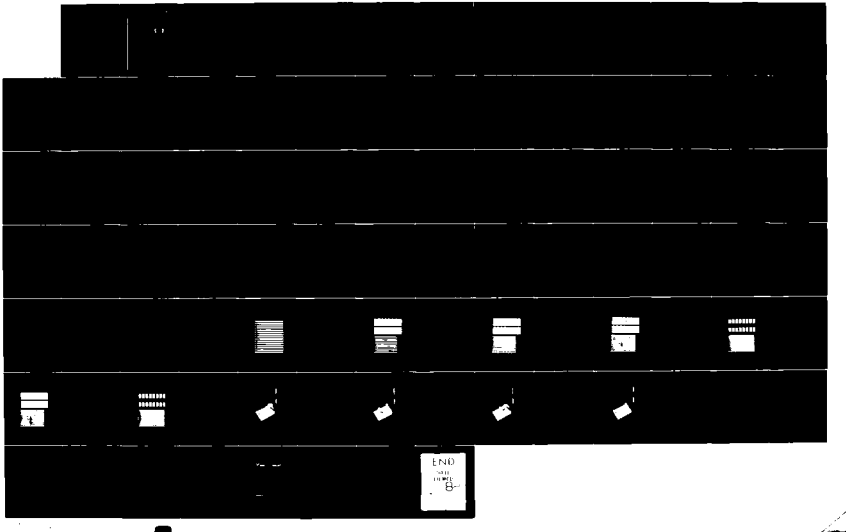

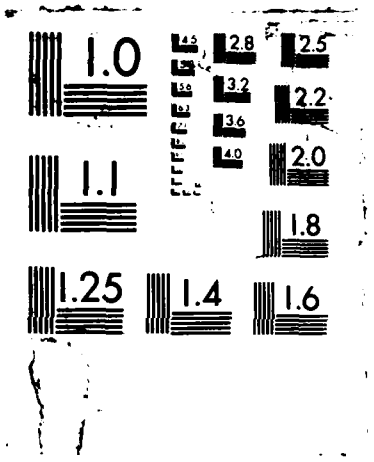
1.0
1.1
1.25
1.4
1.6
1.8
2.0
2.2
2.5
2.8
3.2
3.6
4.0
4.5

SACLANTCEN REPORT
serial no.: SR-112

SACLANT ASW
RESEARCH CENTRE
REPORT

Low-frequency reverberation measurements with an activated towed array:

Scattering strengths and statistics

D. Marandino

October 1987

The SACLANT ASW Research Centre provides the Supreme Allied Commander Atlantic (SACLANT) with scientific and technical assistance under the terms of its NATO charter, which entered into force on 1 February 1963. Without prejudice to this main task—and under the policy direction of SACLANT—the Centre also renders scientific and technical assistance to the individual NATO nations.

Page count for SR-112
(excluding covers)

Pages	Total
i-iv	4
1-44	44
@1-@38	38
	86

SACLANT ASW Research Centre
Viale San Bartolomeo 400
19026 San Bartolomeo (SP), Italy

tel: 0187 540 111
telex: 271148 SACENT I

NORTH ATLANTIC TREATY ORGANIZATION

SACLANTCEN SR-112

Low-frequency reverberation measurements with an activated towed array:

Scattering strengths and statistics

D. Marandino

The content of this document pertains to work performed under Project 02 of the SACLANTCEN Programme of Work. The document has been approved for release by The Director, SACLANTCEN.

Ralph R. Goodman
Director

Original contains color plates: All DTIC reproductions will be in black and white

intentionally blank page

Low-frequency reverberation measurements with an activated towed array:

Scattering strengths and statistics

D. Marandino

Abstract: Results of reverberation measurements made with a low-frequency activated towed array sonar system in two deep-water locations of the Mediterranean Sea are presented. Measurements took place under a variety of environmental conditions: the frequencies used, in the sub-kiloherts regions, were in two bands around 370 and 740 Hz. Monostatic reverberation data were collected with a variety of waveforms (pulsed continuous wave and linear frequency modulated pulses) in order to obtain an adequate sample of the scattering function. The build-up of the data base has stressed data collection under possibly typical operational conditions for further performance analysis studies.

Preliminary findings of the data analysis indicate that volume reverberation does not seem to be significant for this experimental set-up and that surface reverberation appears almost always overshadowed by seafloor scattering. Bottom scattering dominates returns through both the so-called fathometer effect and direct backscattering from the range of grazing angles. Scattering strengths appear independent of frequency and spectral histories show no significant doppler shift. Long-range returns are dominated by bottom highlights. Reverberation time series, which are highly non-stationary, can however be assumed to be locally covariance stationary, and logarithmic normalization techniques could usefully be applied.

Keywords: ambient noise o Balearic basin o bottom backscattering o bottom reverberation o boundary reverberation o fathometer effect o grazing angle o long-range backscattering o low-frequency reverberation o scattering strength o surface backscattering o surface reverberation o Tyrrhenian sea

Contents

1. Introduction

This report presents results of reverberation measurements made with an activated towed array and a related analysis based on a comparison with model predictions. The measurements were made in various deep water locations of the Mediterranean Sea and under a variety of sea-states. The transmisssion frequencies used, in the subkilohertz region, were located around two bandwidths centered at 370 Hz and 740 Hz. Monostatic reverberation data were collected using a variety of waveforms (continuous wave and frequency modulation types) in order to obtain an adequate sample of the reverberation scattering function.

The task was undertaken in support of on-going studies at SACLANTCEN which are investigating, both theoretically and experimentally, the potential for long-range detection using a sonar based on the low-frequency activated towed array concept. As with any high-power active sonar system, reverberation represents a serious system performance limitation which must be taken into account.

Consequently a programme of measurements was generated with an emphasis on low-frequency reverberation; in addition, as the activated towed array concept is new the desirability of collecting operational data under typical environmental conditions is urgently required.

The objective has thus been to generate a database of reverberation returns which not only yields first and second order parameters such as reverberation types, scattering strength values, spectral characteristics and statistics, but also provides inputs for further studies on detection, classification and tracking in a reverberant environment.

The programme has up to now had a strong experimental bias. Considerable effort has been devoted to collecting a sizeable and reliable database for reverberation returns for a low-frequency activated towed array under a variety of operational and environmental conditions. The initial data analysis has led to seafloor backscattering being identified as the dominating source in the reverberation process; in addition, bottom backscattering strength data for typical areas have been evaluated. An associated statistical analysis indicated that reverberation for this class of sensors tends to be locally covariance stationary, and therefore logarithmic normalization techniques can be usefully applied.

The report commences with a description of the experimental set-up and of the data processing. A review of the theory of reverberation and of the principles of computer prediction models with a reverberation capability follows, and then the

current theoretical approaches, and related formulas for estimating reverberation characteristics are summarized. In the presentation of the results typical experimental data are given in the form of real-time colour displays of recorded intensity time series of beamformed outputs for various waveforms. A preliminary analysis is made of the relevance of bottom backscattering and of the statistics of the intensities of both ambient-noise dominated data and reverberation-dominated data. The conclusions of the analysis are recapitulated and summarized in the final section.

2. The experimental set-up and data processing

Monostatic reverberation measurements were obtained by transmitting acoustic pulses from a high-power towed sound source, and receiving returns on the SACLANTCEN Prakla-Seismos horizontally towed linear array. Figure 1 shows the system layout for reverberation measurements. Transmission and acquisition were performed while SACLANTCEN R/V *Maria Paolina G.* (MPG) steamed along stable, straight courses, with a constant speed of, usually, 5 kn, along a variety of headings.

The arrangement used, although not optimal for scattering-parameter estimation, was selected as the best way of generating results close to the reverberation that would be measured under the operational conditions for this type of sensor.

2.1. GEOGRAPHICAL AREAS AND ENVIRONMENTAL DATA

The trials were conducted in the Mediterranean Sea at the geographical locations indicated in Fig. 2. Two general areas were involved: the Balearic Basin and the South Tyrrhenian Sea.

- The Balearic Basin is a region typical of the Mediterranean Abyssal Plains and features a rather homogeneous seafloor structure. A description of the geophysical and geological characteristics of the basin can be found in Ref. [1]. The top layers of the seabed are made up of clay, and clay/silt/sand combinations. Core samples previously collected in the area, see Fig. 3 from Ref. [2], show also the presence of top layers of sand. The bottom depth is very slowly changing over long distances, with rates of less than 1 m per mile in the measurement region, and an average water depth of about 2770 m; this makes the area convenient for comparison with model predictions. (The presently available reverberation prediction models do not allow for a varying bottom depth.)
- The South Tyrrhenian Sea is also a deep water basin, with a maximum water depth of about 3500 m, but it features a complex seafloor structure with several peculiarities such as sea mounts and pinnacles, and several islands all, of volcanic origin.

The measurements were conducted under winter and summer environmental conditions in order to assess velocity profile effects on reverberation returns. Figure 4 shows sound speed profiles over 3000 m of depth, with an expanded view over the first 500 m. The data relate to early April and early September and thus are reaso-

nably typical of average winter and summer conditions. Three shallow-depth XBTs (T4 type, to a depth of 400 m) were made per day.

As is known, in summer the Mediterranean Sea features a pronounced, relatively shallow sound channel with a minimum around 85 to 150 m. This channel is surmounted by a mixed layer from the surface to a depth of about 50 m, sometimes exhibiting small surface ducts. For this situation, surface convergence zones for a source and receiver in the axis of the sound channel are approximately spaced 35 km apart, about half the spacing for an Atlantic summer environment. In winter the conditions are characterized by a negative velocity gradient which gives rise to an upward refracting profile, although a minor surface layer may be present.

Measurements were made with a pretty well distributed set of wind speeds and sea-states, ranging up to sea-state 6 (with wind gusts of up to 45 kn). Sea-state 5 or 6 is the limit for safe operations, for the launching and retrieval of the projector.

2.2. SEA TRIAL CHRONOLOGY AND TRANSMITTER DATA

Table 1 gives a summary of the chronology of the Sea Trials. The table also provides information on the features of the various sources deployed, since the source is the most important element in reverberation measurements.

TABLE 1
Chronology of sea trials and transmitter data[1]

Date	June '83	April '84	Sept. '84	Sept. '85
Duration (days)	4	4	1	5
Area[2]	ST	BB	ST	ST-BB
Type[3]	HX-90R	f.t.	f.t.	f.t.
Configuration[4]	single	b.b.	b.b.	vertical dipole 1.92 m spacing
Level (dB/μPa/1 m)	203	209	209	215 (at 370 Hz) 200 (at 740 Hz)
Pattern	omni	omni	omni	dipole (at 370 Hz) omni (at 740 Hz)
Frequency (Hz)	333	370	370	370-740

[1] Depth: 100 m (nominal).
[2] ST: South Tyrrhenian; BB: Balearic Basin.
[3] f.t.: flextensional transducer.
[4] b.b.: back-to-back.

A detailed description of the history of the evolution of the transmitters can be found in Ref. [3]. Initially a single HX-90R that resonated at 333 Hz was available, and this was followed by a source made out of two flextensional transducers connected in a back-to-back arrangement and resonating at 440 Hz. This configuration, although providing a higher source level, was nevertheless solely omnidirectional. During the September '85 Sea Trial, a new towed-body sound source was introduced, still with two flextensional transducers, but along a vertical axis with a separation of 1.92 m. In the elevation plane the transmission pattern of this source corresponds to a dipole with approximately −20 dB sidelobes at a measurement frequency band centred around 370 Hz. This same configuration was also used for measurements in a high frequency band (740 Hz centre frequency); in this case the pattern was essentially omnidirectional except for a null at ± 35° elevation. The cable length was such that the source trailed the towship by about 450 m.

2.3. DATA ACQUISITION SYSTEM CONFIGURATION

Monostatic reverberation returns were acquired on the Prakla-Seismos towed array. The array was kept at a nominal depth of 100 m and at a horizontal separation from the towship of 900 m. The hydrophone configuration consisted of a 32-element array at both frequencies (370 and 740 Hz); however the hydrophone spacing was 1.96 m (half-wavelength frequency at 382 Hz) for measurements at 370 Hz, and 0.98 m (half-wavelength at 765 Hz) for measurements at 740 Hz. Sensors monitor the array head and tail depth and orientation. A simplified block diagram of the data acquisition system is given in Fig. 5. The hydrophones' preamplified output voltages are relayed in parallel to the acquisition and processing system aboard the towship, where the signals are amplified, filtered, digitized and beamformed; they are also recorded in digital format, on a Bell and Howell High Density Data Recording (HDDR) unit for subsequent off-line analysis.

The Signal Conditioning Unit (SCU) performs analog filtering and amplification (in discrete 6-dB steps), in parallel, on the hydrophone voltages. The filter bandwidth is selected to prevent aliasing in the following analog-to-digital (A/D) conversion. The SCU gain was adjusted with a trade-off between maximum sensitivity and linearity before filtering. A bank of programmable passband filter-amplifiers was added from the September '85 Sea Trial, which allows an increase in gain within the (narrow) signal bandwidths.

The analog voltages are digitized by a bank of 11-bit A/D converters in the Front End Unit. The sampling frequency is chosen to be at least three times the maximum transmitted frequency. The digital samples are stored on the HDDR unit for off-line processing. For real-time processing, the data are fed to WARP (i.e. the Wide Application Real-Time Processing) system.

The WARP consists of an interpolator, a beamformer and a CSPI MAP (Macro

Array Processor) with a fast one-megaword RAM, called the DataRam. These devices are supervised by a Hewlett-Packard HP-1000 minicomputer system with standard disk and magnetic tape peripherals. This chain performs time domain beamforming and matched filtering on the hydrophone time series.

The interpolator consists of two cascaded banks of parallel linear-phase programmable filters. The first stage is actually used to band-pass filter the input data. A typical filter response, including finite word length quantization errors, is shown in Fig. 6a. The second stage does up-sampling for beamforming, by zero padding and low-pass filtering.

No direct complex demodulation is applied to the input data; instead, a sequence of filtering, up-sampling and decimating operations is used to translate the signal down to baseband. This requires the various sample rates to be congruent (i.e. all integer multiples of one another). The driving parameter is the bandwidth of interest, which presently has a value of 35 Hz at 370 Hz and 40 Hz at 740 Hz (as a consequence mainly of projector limitations). As a result, the final sample rates are respectively 70 and 80 Hz.

To accurately form beams with a fine-grain angular resolution, a high sample rate must be selected at the beamformer input. Typically, a resolution of 0.1° in azimuth requires, at 370 Hz, a sample rate of about 13 kHz. The interpolator is therefore used to raise the input frequency, which is relatively low due the constraints imposed by the A/D converters and HDDR. In addition, it is also used to prefilter data in order to allow decimation at the beamformer output as a mean of avoiding aliasing. Consequently, the data rate at the beamformer output is substantially reduced. A further decimation of the various beam time-series takes place in the array processor, after which matched filtering and spectral analysis are applied.

The schematic below shows the sample rates at the various stages, for both frequency bands; Fig. 6 b,c shows the shape of the anti-aliasing filters in the interpolator and in the array processor, for the low-frequency band (around 370 Hz). This selection, which results in a set of beam time series sampled at the Nyquist rate, is determined by a number of trade-offs related to various practical factors such as device dynamic range and performance limitations and word length and number of coefficients.

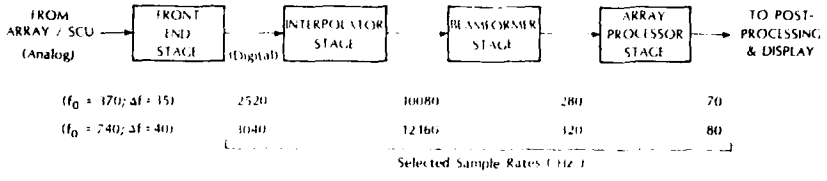

The beamformer performs shift-and-add time domain beamforming on the hydrophone inputs, which generates parallel beam output time series, with optional shading. The beamforming arrangement that was most frequently used consists of 16 beams panoramically pointing into the left/right ambiguous 180° horizontal space, from front to rear endfire. *Hamm shading* is applied to all the beams; this is to reduce sidelobes at the expense of widening the main beam (by about one and a half times). At broadside, the 3-dB beamwidth is thus about 5.4°. A typical beam configuration as determined by the conical symmetry of a linear array is shown at Fig. 7 (horizontal view and side view. The beam arrangement is such that it keeps beam overlap as constant as possible. Two representative beam patterns, at broadside and at endfire, are given at Fig. 8.

2.4. WAVEFORMS AND SIGNAL PROCESSING

In order to adequately sample the reverberation scattering function, continuous wave (CW) and frequency modulated (FM) waveforms were employed to investigate reverberation characteristics signals having good range and good doppler resolution capabilities.

As a practical example, Table 2 lists the characteristics of typical transmitted signals. The codenames shown refer to the real-time colour displays of Sect. 4.

TABLE 2
Parameters of typical transmitted waveforms

Codename[1] (at f_0)	M1 (at 370 Hz) M7 (at 740 Hz)	CF (at 370 Hz) F7 (at 740 Hz)
Type	CW + FM	CW + FM
Pulse length	8 s / 8 s	1 s / 1 s
Swept bandwidth (FM signal)	10 Hz	10 Hz
Repetition rate	240 s	160 s

[1] Ping-to-ping frequency diversity was applied.

The following remarks must be noted:

(a) Use is made of 'composite' signals, whereby each transmission consists of two consecutive sub-pulses (at separate frequencies): a CW pulse followed by a linear FM pulse of equal duration. This allows direct comparison of the scattering characteristics of the environment when waveforms with contrasting capabilities (high doppler, poor range resolution for the CW pulse; vice versa for the FM pulse) are simultaneously propagating into the medium.

(b) Long-duration signals are exploited because long-range detection is one of the primary aims of an active sonar system based on the activated towed array concept. *This makes it more difficult to separate the various scattering processes.*

(c) Low repetition rates and ping-to-ping frequency diversity are required in order to avoid multiple-time-around (or range) ambiguities. The range ambiguities associated with major bathymetric features and coastlines are a severe problem for a high-power active sonar, particularly if they lie in the sound channel in relatively small basins (up to a few hundreds miles across), such as those in the Mediterranean. It is because low repetition rates do not completely overcome the problem that use in also made of frequency diversity, whereby each successive ping is transmitted on a different center frequency, within the available bandwidth of the transducer. The combined effect is elimination of the range ambiguities, as is apparent from the real time coloured displays discussed in Sect. 4.

On reception, the array processor applies conventional matched filtering to the beamformer outputs. Beamformer data are de-multiplexed into the constituent beam time series, which are then individually filtered and correlated. The selection of the processing parameters is such as to adequately sample the delay/doppler ambiguity plane and is made according to Ref. [4].

CW processing. CW processing evaluates the spectral time history of the individual beam data (on a ping-by-ping basis) by computing time-overlapped *Hanning shaded* power spectra. The spectra are obtained by means of Fast Fourier Transform (FFT) algorithms which are taken for time windows that have the same length as the transmitted signal duration and are zero-padded to the appropriate length and evaluated over data segments that have 50% overlapping in time.

Towship motion compensation, or *own doppler nulling* (ODN), is applied to the CW data by realigning the received power spectra as a function of the beam pointing direction and the ship's velocity vector, according to the formula

$$f_d = \frac{2V_{ship}}{\lambda} \cos\gamma, \tag{1}$$

where f_d is the doppler frequency (Hz), monostatic case; V_{ship} is the ship speed (m/s); λ is the acoustic wavelength (m); γ is the angle between ship velocity vector and beam pointing direction.

By applying a correction equal to $-f_d$ all returns from *non-moving* targets which are located along the maximum response axis (MRA) of each beam pointing direction will have spectra centered at zero doppler shift. This is true regardless of the actual location of the scatterer on the three-dimensional MRA curve, which for a linear

array is a cone with its axis along the array axis. (However the realignment is in practice seldom perfect due to the ODN algorithm being unable to compensate for ship-motion fluctuations (or deviations) from the indicated value and transmit-to-receive velocity variations, with the latter deficiency being the most significant.)

The motion of the towing platform thus introduces, for every beam, a relationship between (a) the spatial displacement of a target with respect to the beam's MRA and (b) the doppler shifted frequency of its received echo. As will be clear later on, this is of importance for returns from major bathymetric features and doppler sensitive waveforms (long CW pulses). For a given beam pointing direction, returns received from an extended scatterer (which may be typical of reverberation) throughout the whole beam pattern will thus be affected not only by amplitude shading but also by a frequency shift as a function of the angle between the MRA and the received scattering area.

For multiple beams formed with a linear array, the frequency spread due to main beam off-MRA returns is approximately independent of the beam pointing direction. This can be shown with the following argument. Since ODN applies a $(-2V/\lambda)\cos\gamma$ doppler compensation, the resulting incremental doppler shift of off-MRA, main-beam returns is

$$\mathrm{d}f_\mathrm{d} = k\,[\cos(\gamma + \mathrm{d}\gamma) - \cos\gamma]\,, \tag{2}$$

where $k = 2V/\lambda$ and $\mathrm{d}\gamma$ is the off-axis angle.

For small $\mathrm{d}\gamma$, it is

$$\mathrm{d}f_\mathrm{d} \simeq k\,\mathrm{d}\gamma\sin\gamma\,, \tag{3}$$

and since for linear array it is approximately

$$\mathrm{d}\gamma_{max} = \text{3-dB beamwidth} \simeq \varphi_{br}/\sin\gamma\,, \tag{4}$$

where φ_{br} = 3-dB beamwidth at broadside if γ is not too close to endfire, and hence

$$\mathrm{d}f_\mathrm{d} \simeq k\varphi_{br}\,, \tag{5}$$

which is independent of γ. For the experimental set-up under consideration here, Eq. (5) gives $\mathrm{d}f_\mathrm{d} = 0.11$ Hz at 370 Hz and $\mathrm{d}f_\mathrm{d} = 0.22$ Hz at 740 Hz.

LFM signals. Linear frequency modulated (LFM) signals are processed through a conventional quadrature replica correlator. The de-multiplexed beamformer outputs are correlated in two quadrature channels with a *Hanning shaded* replica in order to reduce range sidelobes effects. No doppler compensation is applied to FM processing since the maximum expected loss for the worst case, such as stationary targets in the endfire beams, is less than 1 dB (due to the fact that the modulation bandwidths used are small).

For both the CW and the LFM signals, envelope detection is applied after matched filtering, by squaring and adding the complex or quadrature channels. The data are further multiplied by a calibration factor which converts values to equivalent dB re μPa pressure level in the processed band, as seen by a single hydrophone. This forms the database for display and further analysis. Therefore the acquisition and processing programs create large arrays of the type

$$\begin{aligned} \Phi_{\mathrm{CW}} &= f(f_i, t_i, \beta_i, \zeta_i), \qquad \text{for CW data,} \\ \Phi_{\mathrm{FM}} &= g(t_i, \beta_i, \zeta_i), \qquad \text{for FM data,} \end{aligned} \tag{6}$$

where Φ_{CW} is the magnitude or complex valued processed CW output; Φ_{FM} is the magnitude valued processed FM output; f_i is the doppler frequency index; t_i is the time-to-transmission index; β_i is the beam index; ζ_i is the transmission number (ping) index.

To keep the storage requirements and computational speed of these large databases manageable, and yet not lose information, the samplings of the time and frequency indexes for the processed output are selected such that for the time increment dt $(= t_{i+1} - t_i)$

$$dt = \frac{1}{\text{FM bandwidth}} \qquad \text{for FM signals,} \tag{7}$$

which gives $\simeq 1.5$ samples per actual 3-dB resolution (due to the Hanning weighting), and

$$dt = \frac{1}{2} t_{\mathrm{p}} \qquad \text{for CW signals.} \tag{8}$$

where t_{p} is the CW pulse duration required by the 50% overlap processing; the resulting theoretical overlap correlation is $\simeq 16\%$ (see Harris [5]).

For CW waveforms, the frequency increment df $(= f_{i+1} - f_i)$, which is the frequency definition of the spectra, is selected such that

$$f = \frac{1}{q_l t_{\mathrm{p}}}$$

in which

$$q_l = \frac{2^N}{f_{\mathrm{s}} t_{\mathrm{p}}}, \tag{9}$$

where f_{s} is the processing sample rate; and N is the nearest larger integer to obtain $q_l \geq 1$; and 2^N is the FFT length. This selection makes the frequency definition (or *bin*) $\simeq 2$ times smaller than the theoretical frequency resolution of the CW waveform (with Hanning shading).

Having defined the selection for the increments of the various indexes, the criteria to specify the size of the databases are based on considerations related to the physical

limitations for maximum transfer rates. These limitations are not described here, but in general the coverage in frequency is such as to have a fixed frequency range at a given carrier irrespective of other waveform parameters (for instance it is 4 Hz at 370 Hz centre frequency).

3. Review of reverberation theory

3.1. INTRODUCTION

Reverberation is the process that describes the time variation of the total scattered sound field observed at a point of reception following transmission of a signal (Ol'shevskii [6]). Thus, it is associated with the intrinsic statistical inhomogeneity of the underwater medium. Reverberation is fundamentally a non-stationary stochastic process.

Reverberation is commonly classified into two categories:

- *Volume reverberation* due to the scattering from inhomogeneities in the ocean medium itself, such as those attributable to biological origin (e.g. the microorganisms of the Deep Scattering Layer, for instance, and fish) or thermal irregularities or, possibly, internal waves.
- *Boundary reverberation* arising from the scattering associated with the interaction of sound with the medium discontinuities represented by the ocean boundaries. This is further classified into:
  - *surface reverberation* caused by the scattering of sound at or near the sea surface, due to ocean surface waves or to entrapped air bubbles, and
  - *bottom reverberation* due to the scattering of sound by the inhomogeneities of the ocean bottom and the irregularities of the bottom surface.

Two theoretical approches have been taken to describe the statistics of the backscattered sound fields. Both approaches, by analogy with the Huygens-Fresnel principle of physical optics, consider the scattered sound field as consisting of elementary waves in mutual phase interference. In the first classical or 'physical' approach a solution of the appropriate dynamical equation of the propagation is searched, introducing the stochastic mechanism of random scattering as a spatial perturbation. This method incorporates the (statistical) parameters of the scattering process into the Helmoltz-Kirchhoff equations for a lossless inhomogeneous medium; it therefore relates the statistics of the scattering mechanism with the *geophysical* bulk parameters of the medium. However its complexity limits its usefulness in handling complex geometries, waveforms and higher-order statistics.

In the second approach, the *quasi-phenomenological* model of Faure [7], Ol'shev-

skii [6], and Middleton [8], a random distribution of independent point scatterers in the medium is introduced in the dynamical equations of propagation. The medium itself is treated as infinite and everywhre homogeneous and isotropic. First order scattering is commonly assumed: that is, the scatterers do not mutually interact and simply reradiate part of the incident field in all directions. This is statistically equivalent to the assumption that the scattering process is a *Poisson* process independent both in space and time. Ray theory is usually invoked to determine geometric boundaries of the illuminated scatterers and the received fields; additionally, the boundary conditions can be expressed by means of a dynamical *impulse response function* which represents the relationship between the incident and reradiated field. Although this approach does not directly relate scattering with physical medium parameters, it handles complex situations and higher-order statistics.

3.2. SCATTERING STRENGTH AND PREDICTION MODELS

In general, the mean reverberation intensity (a function of time) depends on the distribution and the characteristics of the scatterers in the illuminated region. Therefore the *time-varying* average is related not only to geometry and system-related factors (such as source power and effective pulse length, transmit and receive beam patterns and sound speed profiles) but also to factors related to the scattering mechanism itself, such as the mean number and the acoustical properties of the scatterers within the illuminated area.

The latter factors are usually expressed by a single parameter, the *scattering strength*, which is a convenient way of quantitatively describing the effect of reverberation. It represents the ratio between the intensity of the sound scattered by a unit area or volume referred to a distance of 1 m and the incident plane-wave intensity. This ratio is commonly expressed in decibels, and for volume scattering is

$$S_{\mathrm{v.s.}} = 10 \log s_{\mathrm{v.s.}} = 10 \log \left(\frac{I_{\mathrm{r}}/\text{unit volume}}{I_{\mathrm{i}}} \right) \tag{10}$$

and for boundary scattering

$$S_{\mathrm{b.s.}} = 10 \log s_{\mathrm{b.s.}} = 10 \log \left(\frac{I_{\mathrm{r}}/\text{unit area}}{I_{\mathrm{i}}} \right). \tag{11}$$

The scattering strength is thus defined in a similar manner to the target strength. It is used in computations of the echo to reverberation level, and three types of scattering strengths can be distinguished according to the different types of reverberation (S_{v} for volume, S_{s} for surface and S_{b} for bottom scattering).

By assuming the scattering strength constant over the incremental area there is considerable simplification of the propagation equations; nevertheless, most situations of practical interest are still too complex to permit a closed-form solution to the problem of estimating the received intensity and thus it is necessary to apply numerical integration techniques. Consequently, one resorts to computer models that include a reverberation prediction capability, such as the GENERIC Sonar Model (Weinberg [9]), NISSM (Weinberg [12]), the NRL Reverberation Model (Franchi et al. [11]) and LIRA (Hoffmann [10]).

The method used by the computer models to estimate reverberation levels is rather straightforward and relies on linear and first-order approximations of the scattering process; that is, no allowance is made for secondary scattering effects (scattering from scattering) or mutual coupling, and the scattering strength over the illuminated incremental area is constant.

The received level at a sensor following transmission of a signal of power P and effective duration t_p is evaluated by considering the closed ray path that is formed between the source and an incremental scatterer, and another to the receiver. The acoustic pressure at the end of this pair of eigenrays is given by

$$I_{rev} = P_s D_s \eta_f s_r \, d\phi \, \eta_b D_r , \tag{12}$$

where P_s is the source power; I_{rev} is the received intensity; D_s is the source directional gain in the direction of the outgoing ray; D_r is the receiver directional gain in the direction of the incoming ray; η_f is the propagation loss in the forward path; η_r is the propagation loss in the backward path; s_r is the scattering strength; $d\phi$ is the incremental scattering area or volume.

Since the effective duration of the signal is t_p, the contribution to the received level comes from all forward and received (multipath) eigenrays which satisfy

$$t_0 - t_p \leq t_f + t_r \leq t_0, \tag{13}$$

where t_0 is the reference time at which the power is measured and t_f and t_r are the forward- and receive-path travel times respectively.

Since the resultant *mean* reverberation pressure level is the random-phase addition of the individual contributors, it is

$$P_{rev}^2 = \int_{\Phi} \int_{t_0 - t_p}^{t_0} |I_{rev}|^2 \, dt \, d\phi , \tag{14}$$

where Φ is the illuminated area or volume.

In the evaluation of the received level account must be taken of all possible paths from the source to the scattering region and back to the receiver. The evaluation

of Eq. (14) is accomplished by a numerical summation over a 'reasonable' number of significant paths and over the illuminated area. Equation (14) also shows that it may be difficult to separate contributions coming from different spatial regions (which are thus of different types) if the travel times of their eigenray pairs fall within the same window; this comment is particularly applicable to long-range reverberation.

The practical complexity of this solution shows how necessary a computer model is for the prediction of the received levels and the prediction of the scattering parameters. However a simplified approach that is useful for first-order parameter assessment can use the standard sonar equation (Urick [13]) in the form

$$\mathrm{RL} = \mathrm{SL} - \mathrm{TL}_2 + S_{sc} + 10 \log \Phi_{sc}, \tag{15}$$

where RL is the received power level (dB re μPa), SL is the source level (dB re μPa), TL_2 is the two-way propagation loss (dB), S_{sc} is the scattering strength (dB), Φ_{sc} is the integral over the scattering region.

Such a simplification is applicable when the various elements of Eq. (15) are separable; and it is convenient to use it when the factors can be easily expressed, as can for instance the propagation loss, by means of an analytical spreading law. However, the *equivalent* scattering region Φ_{sc} must be estimated as a function of the transmission parameters and of the source and *receiver beam patterns*.

3.3. VOLUME *vs* BOUNDARY REVERBERATION AT LOW FREQUENCY

Volume reverberation is mostly of biological origin, and is commonly associated with the Deep Scattering Layer; therefore volume scattering, at the low end of the frequency spectrum (down to 2 kHz), is most likely caused by resonance effects from the gas-filled swimbladders of the larger types of fish. At low enough frequencies, below 1 kHz, where wavelengths are in the order of more than 1 m, volume scattering strength can therefore be expected to be small.

Measurements of S_v in the Mediterranean Sea (Doutt [14], lowest frequency analysed 1.6 kHz) showed the spectral behaviour as peaking at frequencies in the range of 4 to 8 kHz. As the measured fall-off rate of S_v *vs* frequency at the lower end was close to the theoretical 40 dB/decade expected from the resonant nature of the scattering from swimbladders, this ruled out the possibility of large scatterers (swimbladder diameters larger than a few tens of cm) having significantly contributed to the scattering process. A value of -110 dB/m for the volume scattering strength has been taken for computer model predictions. This is a conservative figure derived by extrapolating from data for higher frequencies with the scattering taking place at the depth of maximum reverberation.

Although the volume scattering strength is much lower than that of the boundaries, it may nevertheless become predominant at long ranges because the ensonified volume may grow large enough with respect to the ensonified areas. The ratio between volume and boundary reverberation at a given distance can be approximately expressed, from Eq. (15), assuming all other factors identical, as

$$\mathrm{RL}_{\mathrm{v.r.}} - \mathrm{RL}_{\mathrm{b.r.}} = S_{\mathrm{v}} - S_{\mathrm{b}} + \left(10 \log \int_{\Upsilon} \Psi(\varphi, \vartheta)\, \mathrm{d}V - 10 \log \int_{\Delta} \Psi(\varphi, \vartheta)\, \mathrm{d}A \right) , \quad (16)$$

where $\mathrm{RL}_{\mathrm{v.r.}}$ is the received level due to volume reverberation, $\mathrm{RL}_{\mathrm{b.r.}}$ is the received level due to boundary reverberation, S_{v} is the column scattering strength, S_{b} is the boundary scattering strength, $\Psi(\varphi, \vartheta)$ is the beam pattern (function of azimuth and elevation angles), Υ is the scattering volume at range R, Δ is the scattering area at range R.

The usual simplifying assumptions for the evaluation of the scattering area and volume show that for an unbounded medium (which is an unrealistic hypothesis for long ranges where the elevation angles are limited by the water depth) the magnitude of the expression within parenthesis in Eq. (16) grows at approximately the rate of $10 \log R$. Now since the ratio between volume and boundary scattering strength can at these frequencies confidently be expected to be at least −50 dB or larger, it follows that volume reverberation may exceed boundary reverberation at ranges of 100 km or more. However, since reverberation decays as a function of range, volume reverberation should exceed boundary reverberation for moderately high source levels that are well below the ambient noise levels.

This is illustrated at Fig. 9 which shows the GENERIC Sonar Model prediction of the reverberation levels for a system configuration and environment simulating the present experimental one. Source and receiver are located in the sound channel; reverberation is estimated for a transmission of a CW pulse of 8 s at 370 Hz and a source level of 213 dB re μPa @ 1 m. Reception at the broadside beam of a 32-element, shaded, towed array is simulated. Commonly-used values for the surface and bottom scattering strengths have been selected from the Chapman-Harris and McKenzie formulas respectively. Volume scattering data have been taken equal to −110 dB/m at the usual deep scattering layer (DSL) depths, as postulated above. The levels for the three forms of reverberation show that volume reverberation can be expected to be some 20 dB below the other forms of reverberation over several tens of kilometers. Volume returns may eventually become larger at those ranges where reverberation levels are well below noise levels. These are the reasons why volume reverberation effects have been neglected in the further analysis of the present data.

3.4. SURFACE REVERBERATION THEORY

The theory of the scattering of sound from periodic or random surfaces is well

established (see Fortuin [15]) with the basic work of Lord Rayleigh [16] and the extensions of, among others, Marsh [17], and the approach of Eckart [19] and Brekhovskikh [20], which are based on the Kirchhoff approximation to the Helmholtz integral of the scattered field induced at the boundary by the incident wave. The *composite-roughness model* for the diffraction effects due to the surface is an approach which presently receives widespread acceptance and essentially merges results from both the Rayleigh-based methods with those based on the Kirchhoff approximation (see McDaniel [21]). Hence, a geometrical optics approximation is applicable (Eckart) if

$$\alpha_r = kh \sin\theta \gg 1 , \tag{17}$$

where α_r is the Rayleigh roughness parameter; $k = 2\pi/\lambda$ is the acoustic wavenumber; λ is the acoustic wavelength; h is the rms surface height (surface roughness parameter); θ is the grazing angle at the surface. And this condition (17) applies for the high-frequency situation as well as for forward near-specular or monostatic high grazing backscatter. This approximation predicts that the scattered field angular intensity is dependent on the *local* specular reflection associated with the surface slope normal to the impinging sound. As a consequence the scattering process is, to a large degree, a coherent phenomenon, with the intensity dependent on the mean square slope of the surface but independent of wavelength.

If however $\alpha_r \ll 1$ as would be the case for low acoustic frequencies impinging upon the surface at small grazing angles, then linear scattering theory (Rayleigh-Marsh) should provide a good qualitative description of the scattered field from a complex boundary ensonified by a plane acoustic wave. This description considers the surface acting like a diffraction grating, and therefore the scattering is essentially resonant. For a purely periodic, infinite surface, scattering takes place in discrete directions, and at discrete frequencies given by

$$\sin\vartheta_s = \sin\vartheta_i + n\lambda/\Lambda , \tag{18}$$

where ϑ_s and ϑ_i are respectively the scattered and incident angles measured from the vertical direction (see Fig. 10); λ and Λ are respectively the acoustic and the surface wavelengths; and n is the scattering order. For $n = 0$ scattering is the 'specular' reflection, and is a coherent process at the frequency of the incident wave; $n = 1$ gives the first-order, diffuse scattering component which is shifted in frequency. The theory shows that the zero order and the first order are the most relevant contributors to the amplitude of the scattered field. Equation (19) reflects the resonant nature of the scattering process, since a given acoustic wavelength will 'select' a particular wavelength of the spectrum of the surface roughness (or a narrow band thereof). The diffuse re-radiation will, however, not be truly discrete due to the randomness and finite size of the illuminated surface. Marsh, Shulkin and Kneale [18]) have extended the analysis to random surfaces, and have computed the values of the first-order scattered field, which turns out to be *a function of the surface wave spectrum only*. The amplitude of the first-order backscattered field is

approximately given by

$$A_1 \simeq \frac{B}{g^2} \sin^4 \theta P^2(\omega_w) \tag{19}$$

where B is a dimensionless constant and $P^2(\omega_w)$ is the power spectrum of the sea surface elevation *vs* wave frequency. If $P^2(\omega_w)$ is assumed equal to the Pierson-Moskowitz sea-state spectrum assumption (see also Fig. 11) then

$$P^2(\omega_w) = \Gamma g^2 \omega_w^{-5} \exp(-0.74 g^4/\omega_w^4 v^4), \tag{20}$$

where g is the acceleration of gravity, Γ is a normalization factor, and v is the wind speed. By neglecting the exponential term in Eq. (20) (for a fully developed sea), A_1 from Eq. (19) should be independent of ω_w and be dependent only on geometrical factors.

These conclusions have several consequences. Firstly, the amplitude of the scattered field should be reasonably independent of the sea-state if the acoustic frequency involved is above roughly 50 Hz, because the selected wave frequency will be approximately independent of sea-state. However, there should be a dependence on the sea-state direction due to the geometrical diffraction mechanism itself. Secondly, since the sea surface is a time-dependent moving boundary, the motion of the ocean waves should impose a frequency shift on the first order scattered field. This doppler effect can be estimated by considering the relationship between surface wavelength Λ and wave frequency f_w. For gravity waves in deep water the surface wavenumber is given by

$$K = \frac{2\pi}{\Lambda} = \frac{\omega_w^2}{g}, \tag{21}$$

where $\omega_w = 2\pi f_w$. By combining Eqs. (18) and (21) and for the predominant first-order scattering ($n = 1$) and assuming $\vartheta_s \simeq -\vartheta_i$ close to grazing incidence ($\vartheta \simeq 90°$), which is the case for reverberation from ranges where $R_s \gg d_{s,r}$ (in which $d_{s,r}$ is the source-receiver depth and R_s is the range from which surface reverberation is received), then

$$|f_d| = \sqrt{\frac{g}{2\pi\lambda}} \sqrt{|\sin\vartheta_i - \sin\vartheta_s|} \simeq \sqrt{\frac{g}{\pi\lambda}}, \tag{22}$$

where f_d is the doppler shift of the backscattered field and appears to be related only to the incident wavelength. This constant shift should be $\simeq 0.87$ Hz at 370 Hz (acoustic frequency) and $\simeq 1.24$ Hz at 740 Hz. The polarity of the doppler shift in Eq. (22) is determined by the sign of the cosine of the angle between the direction of the incident energy and the predominant sea direction.

The overall behaviour of the scattering strength as a function of the grazing angle is therefore expressed by the composition of two curves representing the two regions

of near specular and diffuse backscatter. There should be little or no frequency dependency for high grazing angles, but it can be expected in the medium to low grazing region. As far as experimental data for low-frequency surface scattering are concerned, the results of Chapman and Harris [22] for diffuse scattering and Chapman and Scott [23] for high grazing angles are in widespread use. (These are the 'default' values of most computer prediction models.) For diffuse scattering (medium to low grazing angles) Chapman and Harris fitted the following formula to their experimental data (to within 2 dB, on average, from the measured values):

$$S_s = 3.3\kappa \log(\theta/30°) - 42.4 \log \kappa + 2.6 ,$$
$$\kappa = 158 \left(\upsilon f^{1/3}\right)^{-0.58} , \tag{23}$$

where S_s is in dB; θ is the grazing angle in degrees; υ is the wind speed in knots; and f is the acoustic frequency in Hz. Note that Eq. (23) predicts a sea-state dependence which is not readily derived from the Rayleigh-Marsh theory. For high grazing angles, Chapman and Scott fitted their data to the Eckart's theory to obtain

$$S_s = -10 \log(8\pi\epsilon^2) - 2.17\epsilon^{-2}/\tan^2\theta ,$$
$$\epsilon^2 = 0.003 + 0.003\upsilon . \tag{24}$$

Figure 12a shows the behaviour of the composite surface scattering strength as predicted by the formulas for a number of frequencies.

3.5. BOTTOM REVERBERATION THEORY

The theory of the scattering of sound from the surface can in principle be equally well applied to the scattering of sound from the bottom. However while the surface can be considered a perfect pressure-release surface, it is only approximately, and only for very hard bottoms, that the seafloor can be considered a perfectly rigid boundary. Seafloor scattering is thus a more complex process and usually requires taking into account the energy that propagates into the sub-bottom layers, and is accordingly much more difficult to predict, particularly at low frequencies, where bottom penetration is more pronounced. Bottom reverberation is therefore commonly expressed as a function of the seafloor geophysical properties (sand, rock, clay or silt) or type, in addition to the seabed roughness.

A composite model can also generally be assumed for the scattering from the seafloor. At medium and small grazing angles a diffuse, incoherent form of scattering as indicated by the linear scattering theory is appropriate, whereas at high grazing angles, a facet reflection model is better. Although first-order bottom scattering is primarily related to the roughness of the seafloor, it is usually not easy to determine the bottom roughness. A common way of relating scattering to grazing angle, at

a given frequency, and in the absence of a description of the bottom structure, is to assume that scattering is in accordance with a Lambert's rule of physical optics for rough surfaces, which assumes the amplitude of the scattered sound to be proportional to the sine of the grazing angle. That is

$$I_s = \mu I_i \sin\theta_i \sin\theta_s , \tag{25}$$

where I_s is the intensity of scattered sound; I_i is the intensity of incident sound; θ_i is the grazing angle at incidence; θ_s is the grazing angle in the scattering direction; μ is the proportionality constant.

Thus the scattering strength (in dB) for the case of monostatic backscattering, where $\theta_i \simeq \theta_s$ is

$$S_b(\theta) = 10\log\left(\frac{I_s}{I_i}\right) = 10\log\mu + 10\log\sin^2\theta . \tag{26}$$

Literature data in general show a qualitatively good agreement with Lambert's rule, see for instance Schmidt [24] and Urick [13]. The behaviour of the bottom scattering strength *vs* grazing angle resulting from the composite model of diffuse scattering expressed by Lambert's rule, with μ equal to -27 dB, and the facet reflection model, is shown in Fig. 12b. Typically, experimental data show an initial, rapid decay for near normal incidence, followed by a plateau region in which S_b does not strongly depend on the grazing angle. At very small grazing angles S_b should decay quickly; however measurements of the scattering strength at very small grazing angles are particularly difficult. Although Eq. (25) is rather empirical, it is nevertheless convenient because it requires the estimation of the single parameter μ which in general can be taken to characterize a bottom type.

Reported values of low-frequency bottom backscattering strength indicate that it is the type of bottom more than its roughness that is indeed the dominating factor. The same data usually show a small or no frequency dependence in the sub-kilohertz region. It is also important to point out that bottom backscattering should exhibit no frequency shift, unlike surface scattering, since the seafloor is stationary.

4. Experimental results

Examples of data sets of reverberation measurements obtained with an activated array towed in deep water are given in Figs. 13 to 19. The data-sets are presented in the form of colour-coded real-time displays of the returns received following the transmission of various composite waveforms. The system configuration is the standard one for a (quasi-) monostatic towed source/array. Table 3 provides a summary of information relevant to the runs which generated the data in the displays. Transmission characteristics are deducible by referring to Table 3, which gives the time of the runs and also geographical and environmental information. The last column in the table is a cross-reference to Figs. 20 and 21, which schematically show the positions of the various runs with respect to the basin boundaries.

TABLE 3
Reference data for the real-time colour displays

Figure no.	Signal[1]	Date/ time (z)	Area[2]	Position (mid-run)	Ship heading	Sea-state	Ref. figure[3]
13	CF	10 Apr. '84, 11:49	BB	41°15′ N, 07°24′ E	010°	2	20-A
14	M1	10 Apr. '84, 15:27	BB	41°35′ N, 07°31′ E	010°	2	20-B
15	M1	24 Sept. '84, 17:02	ST	39°26′ N, 13°08′ E	180°	3	21-A
16	M1	4 Sept. '85, 09:37	ST	40°14′ N, 12°36′ E	300°	2	21-B
17	M7	4 Sept. '85, 10:41	ST	40°16′ N, 12°29′ E	300°	2	21-C
18	M7	6 Sept. '85, 08:06	BB	41°48′ N, 07°40′ E	010°	4	20-C
19	M1	6 Sept. '85, 10:58	BB	42°00′ N, 07°45′ E	010°	4	20-D

[1] Refer to Table 2.
[2] BB: Balearic Basin; ST: South Tyrrhenian.
[3] See text.

Figure 13 displays only the processed FM data of the composite signal CF. The figure shows a multi-ping, multi-beam real-time colour-coded display. *Two-way slant sonar range*, expressed in km, is displayed vertically and the various beam

pointing directions (refer for instance, for the first two figures, to the beamformer set-up at Fig. 7) are given horizontally; 0° is forward endfire, 90° is broadside and 180° is rear endfire. Each beam/range set is made up of sequential-pings data. The received power level is expressed in *calibrated* dB **re** μPa at the output of the matched filter and is colour-coded according to the scale at the lower right hand side in the figure. Since echoes are recorded with a moving platform, non-moving targets generate 'tracks' on this multi-ping display, with geometries that are related to the relative viewing angle from the towship. For instance, over short time intervals, when a target remains within a single beam, a fixed target will appear moving inward if at the forward endfire, outward if at the rear endfire, and at constant range if at the broadside beam. Over longer time periods, a fixed target will also move from beam to adjacent beam.

The other figures, which pertain to the composite signals M1 (at 370 Hz) and M7 (at 740 Hz), include both FM and CW displays. The FM display on the left side is identical to that of Fig. 13. The CW display, on the right side, shows the *received power spectrum* for each beam as a function of range, and thus gives the spectral time history of the CW returns. The various beam looking directions, which are the same as for the FM display because the returns are transmitted, received and processed simultaneously, are arranged as a cascade of smaller displays of received intensity versus two-way sonar range and frequency (doppler shift). The range (or time) variable, which runs vertically, covers the same extent as in the FM display. Ping-to-ping exponential-decay averaging is applied to the data and the number of pings used for averaging is given by the parameter AV in the figure. Usually a small number of pings (3 or 4) for the running average is sufficient to smooth noise and reverberation, thus providing a reasonably stable and uniform pattern that slowly changes as a function of the environment. As in the FM case, the display shows calibrated colour-coded power levels at the output of the processor. There is no need to rescale the results since both signals have the same duration and hence the same energy, and they therefore perform identically against a white gaussian-noise background. ODN is applied to the CW data; all stationary scatterers in the main beam of any beam looking direction provide returns which are centered at zero doppler shift.

The most prominent features of the reverberation, and its relationship with the transmitted waveform, are readily apparent from the figures, which show the result of *linear processing* of the received intensities in both space and time. The ambient noise over the period of a run (usually about one hour) appears generally anisotropic, and non-stationary due to towship noise contamination and to medium-range or nearby shipping contamination. The initial returns have very high levels, which are larger the closer the beam is to broadside, and progressively decay, depending to some extent on the waveform characteristics, below the average ambient noise level. LFM waveforms, with higher range resolution, show that the structure of the initial returns is dominated by regularly spaced 'peaks', which are associated with the multiple bottom-surface reflections (the so-called fathometer effect). Long-range

echoes are always easily related to the backscattering from the basin boundaries (as a visual comparison of the figures with the locations of the runs confirms) or to seafloor highlights such as seamounts. The next section amplifies the data analysis and gives further interpretation of the results.

5. Interpretation of results and model comparison

In Subsect. 3.3 it has been shown that volume scattering did not play an important rôle in this experiment and therefore it has not been considered further.

As far as boundary reverberation is concerned, it was possible through analysis and interpretation of the data to derive the conclusion that surface reverberation effects were lower than one might have expected. It was also concluded that the experimental set-up was not sensitive to surface scattering and therefore it was essentially not useable for estimating surface scattering strength values. On the other hand the measured low-frequency reverberation data were clearly dominated by bottom scattering, which in turn affected the returns in the various ways described in this section. Prior to the description however, a discussion is given of the reasons that led to the rejection of the surface-scattering data.

5.1. SURFACE AND BOTTOM BACKSCATTERING EFFECTS

The approach taken in the identification and separation of the surface and bottom contributions had two elements: (a) comparison with, and analysis of, computer model predictions, and (b) clues provided by linear scattering theory.

(a) The computer model analysis was mainly made with the GENERIC Sonar Model [9] since this was regarded as the most complete model available for reverberation predictions. More recent programs, such as the NRL Reverberation Model are possibly more tailored to the analysis of the data that were obtained, but they were unavailable at the time of the analysis.

(b) With regard to the search for clues provided by linear scattering theory, it was decided that as criteria for separating the two processes time and frequency discriminants could be used. Since long-duration waveforms were used (minimum pulse width 1 s), separation in time was really only applicable before reception of the first bottom bounce. After that, surface and bottom returns overlapped. Frequency thus seemed possibly to be the best discriminant. Since the conditions of the experiment were such that the Rayleigh parameter was less than unity, the theory in Subsect. 3.4 indicated that surface scatter ought to be doppler shifted by a fixed amount dependent on the carrier, whereas bottom scatter would have to be at zero doppler shift (assuming towship motion compensation to be applied).

The version of the GENERIC Sonar Model that was available (version C) represents a considerable improvement over the older NISSM model, but nevertheless

retains some limitations which must still be taken into account when comparing predictions with real data. The most relevant are the following: the model assumes an environment independent of range and time, that is, a flat bottom and a horizontally stratified ocean (constant sound speed profile *vs* range). Sloping of the bottom, which has been recognized as an important factor for bottom reverberation [11], is not accounted for. Additionally, GENERIC does not adequately model the three-dimensional beam patterns of a linear array, and does not have bistatic,i.e. non-colocated, source and receiver modelling capability. Nevertheless, since comparisons have been purposely made with appropriate environments such as the Abyssal Plains, the model indications are considered acceptable. An example of the GENERIC Sonar Model predictions tailored to the experimental conditions, is provided at Fig. 9, in which the reverberation predictions are presented for the set-up used during the September 1985 Sea Trial, with simulated transmission of an 8 s, 370 Hz CW pulse in sea-state 4 and reception at the broadside beam.

Inspection of the results obtained with signals that had good range resolution (tens of meters) shows that before reception of the first bottom bounce the data in all beams appear to include ambient noise alone, i.e. the presence of surface reverberation is not evident. See for instance data at the initial ranges in Fig. 13.

After the onset of the first bottom bounce, reverberation returns, although decaying as a function of distance, were up to 50 dB above the ambient noise level at the initial ranges. The closer that beams were to broadside the higher the received levels. The fact that these beams were receiving backscattered energy from the seafloor more directly (because of the conical symmetry of the patterns) is an indication that bottom reverberation dominated other forms of scattering. If surface scatter were to dominate, the intensities would, contrary to the experimental observations, be increasing with increasing angle from broadside, particularly in the convergence zones, which is also shown by model predictions.

Conclusions drawn from the received power levels are, however, not too reliable—mainly because the fathometer effect (to be discussed later) may well overwhelm all other processes, but also because the bottom and surface reverberation levels are not too different, as indicated by computer predictions. The predictions at Fig. 9 were obtained by entering scattering-strength values from the standard formulae of Chapman-Harris and McKenzie. It can be seen that although bottom returns almost always exceed surface returns, except in the convergence zone, the difference is consistently marginal (only a few dB). This is because the Chapman-Harris formula, unlike linear theory, predicts a strong dependence of S_s with sea-state (or wind speed). From sea-state 2 to sea-state 4 the predicted increase of the scattering strength at medium and low grazing angles wasis approximately 25 dB.

The use of frequency as a discriminant relies on the analysis of waveforms with high doppler resolution. The spectral analysis of long CW signals does not indicate the presence of doppler shifted peaks in the received spectrum time history of the va-

rious beams, which would be predicted if surface scattering were present. Refer for example to Figs. 22 to 25. These are contour plots of ensemble-averaged spectral time histories of the returns following an 8 s, 370 Hz CW transmission. The figures show data for two beams, broadside and rear endfire, and for two different sea-states: sea-state 2 (average wind speed less than 7 kn) and sea-state 4 (wind speed > 20 kn). Although the locations on the two days were different, it was essentially the same environment (as regards seafloor depth and structure) and velocity profile (summer; Mediterranean; deep-water). It is apparent from the broadside data that the peaks of the spectra all lined up at zero doppler shift and that there is no significant secondary lobes at the frequency shift of 0.8 to 0.9 Hz, as postulated by the diffraction grating equation (see Eq. (18)). At endfire, the received levels, initially much lower than the corresponding broadside data, show shifted spectral maxima at the initial ranges which, however, soon move to the zero frequency shift position. As at broadside, there is also at endfire a lack of significant secondary doppler shifted lobes. In all the figures the insets reaffirm these findings by showing the spectrum for a particular range at which a possible maximum of the surface reverberation could have been observed, as predicted by computer modelling. This corresponds to the first convergenge zone. The spectra are also, in this instance, centered at zero doppler shift and are also quite symmetrical, with no pronounced side peaks. The figures thus confirm the hypothesis that the bulk of the backscattering comes from the seafloor. Bottom scattering is received directly at the broadside beams and is received, in the beams towards endfire, initially through the sidelobes, and then in the mainbeam when scattering originates from that portion of the seafloor that intersects the main beam. This readily explains the doppler shifted initial data, which are due to the lack of doppler compensation by the ODN algorithm (see the discussion at Subsect. 2.4). This is also in good agreement with model predictions.

Another important finding that points to a surface scatter lower than predicted by standard formulae, is the general observation that the returns are essentially independent of not only the sea-state (as shown in the previous figures) but also of the sound velocity profile. Figure 26 shows returns recorded under very similar conditions but in different seasons (winter and summer profiles) and yet they produced very similar results. Note that the winter conditions ought to emphasize surface reverberation because the SSP is essentially totally upward refracting.

In summary, it is concluded that surface reverberation did not affect the presented results and that scattering from the seafloor dominated returns. However the surface still had a profound effect on the received process by modulating the forward and backward travelling rays associated with bottom scattering (Roderick and Cron [25]). This explains the high tails of the sidelobes of the received spectra. These are, however, centered at zero doppler shift and mostly have a 3-dB bandwidth (after matched filtering) within the expected theoretical limits.

Bottom backscattering, which dominates returns of low-frequency, high-power, long

duration waveforms, is a complicated, non-planar process. It appears, however, to be quite clearly separated into two distinct processes, in agreement with the boundary scattering theory previously discussed. These are

(a) a near-specular, reflected component referred to as the fathometer effect, and

(b) a diffuse, incoherent component representing bottom backscattering coming from progressively smaller grazing angles.

The separation of the two contributing processes is evident only if the transmitted waveform has enough resolution capability in time. To illustrate this for a 10 Hz linear FM signal, a typical example of the two separate processes is presented as Fig. 27a,b (from Ref. [26]), which plots the ensemble averaged received intensity time history recorded at the broadside beam (90°) and at beam direction 128° (from forward endfire), over the initial 20 km. The effects associated with the contributing processes are readily evident in the figure: one is the regularly spaced peaks whose positions are beam independent, and the other one is the progressive decay of the received levels as a function of time, observable in between the peaks. For the 128° beam, the decay of the received power levels *vs* time associated with the seafloor scattering at progressively smaller grazing angles only begins after the backscattered energy is received into the main beam (the peak is marked by an arrow on Fig. 27b).

5.2. THE FATHOMETER EFFECT

The fathometer effect arises from the energy that is radiated by the source in the near-vertical direction, and that propagates vertically in the water column, repetitively bouncing off the bottom and the surface. This gives rise to the regularly spaced peaks (the fathometer peaks), whose range separation is equal to the water depth. The peaks are clearly visible in Fig. 27a and in the FM displays of all the figures referred to in Sect. 4. The fathometer peaks are obviously more evident at the broadside beam, but are also present, although attenuated, through the spatial sidelobes, in all other beams, as shown at Fig. 27b.

The fathometer effect essentially involves a reflection process with the elementary areas of the ensonified surface that are normal to the incident sound. Then to a first order of approximation a loss factor is all it takes to describe the process. Indeed, the received level at the fathometer peak can be expressed by

$$P_n \simeq \mathrm{SL} - \mathrm{TL}_n - nL_b\,, \tag{27}$$

where P_n is the received power level at the nth bottom bounce (dB re μPa); SL is the source level (dB re μPa); TL_n is the transmission loss (dB) = $20\log(2n\,d_w)$ for spherical spreading; d_w is the water depth (m); L_b is the bottom loss at normal in-

cidence (dB). It has been assumed that the surface loss and volumetric attenuations are negligible, since frequencies are well below 1 kHz.

Thus L_b can be evaluated, for instance, by

$$\Delta_P = E(P_n) \quad E(P_{n+1}) = 20 \log \left(\frac{n+1}{n} \right) + L_b , \tag{28}$$

where the decay between successive fathometer peaks, Δ_P, is obtained by taking *ensemble averaged* consecutive fathometer peaks.

Normal-incidence bottom-reflection loss estimates made in this way indicate, for the measurement area in the Balearic Basin, values of 5 to 8 dB per bounce (at 370 Hz), which are in good agreement with acoustic reflectivity measurements made in the same areas (Hastrup and Akal [27]).

5.3. BOTTOM BACKSCATTERING vs GRAZING ANGLE

Since bottom reverberation is the principal contributor to the received reverberation levels, use can be made of the received intensity time history to determine bottom scattering strength versus grazing angle. For that purpose, however, it is necessary to avoid the contaminations caused by the fathometer effect. Marandino and Goldsberry [26] discuss a method of determining bottom scattering strength versus grazing angle by taking advantage of the multiple beamforming capabilities of the towed array and processor. This technique offers the advantage of evaluating scattering strength at local maxima of the ratio of reverberation to ambient noise while at the same time avoiding fathometer contamination. The method requires the use of waveforms with relatively high time resolution, capable of clearly separating surface bounces from the direct returns and using information in the beams that are off broadside. The reference describes this technique in detail and gives an example of the evaluation of the bottom scattering strength versus grazing angle at 370 Hz for an area of the Balearic Basin. The same result, expanded to include measurements made in the same location in the 740 Hz band, is given at Fig. 28. These results are presented here in support of conclusions that are not derived from this data set alone. First, the general behaviour of S_b versus grazing angle indicates again that for seafloor scattering a composite roughness model is applicable, with a strong reflective component in the near-specular region and a diffuse process for medium to low grazing angles, where the scattering strength does not seem to depend much on the grazing angle. A Lambert's rule does not adequately describe the medium and low grazing angle region with a single parameter. A best estimate for μ (see Subsect. 3.5), acceptable down to about 20°, is −34 dB. This value, although within range of reported values, is lower than expected for the scattering from the Abyssal Plains. Finally, the data indicate that the scattering strength in the sub-kilohertz region shows no frequency dependence, which is in agreement with the results of Berkson et al. [28].

5.4. COMPARISON WITH MODEL PREDICTIONS

As previously pointed out, the GENERIC Sonar Model [9] was considered the most appropriate model for reverberation predictions in relation to the present experimental set-up, and has therefore been extensively used for simulations.

Of more value than the exact numerical forecasting of reverberation, which is bound to be highly dependent on the detailed environmental and systematic related conditions, is the model's provision of a key to the parameters which are relevant in the predictions.

The version of GENERIC is essentially bi-dimensional and thus does not allow precise modelling of the effect of a three-dimensional beam pattern on the returns. Therefore no agreement is found for comparison with data from endfire beams, although surface reverberation is possibly correctly modelled. For broadside beam data however, where a two-dimensional model is adequate, the agreement is generally more satisfactory.

Because of the significance of the scattering from the seafloor, modelling is useful in revealing how critical the correct estimation of both forward (bottom loss) and backward (scattering strength) parameters is for obtaining a good agreement between measured and predicted values. Whenever the forward and backward parameters have been completely determined the agreement is particularly satisfactory, as shown in the Figs. 29 and 30. These figures show GENERIC predictions superposed on actual data, for reverberation returns measured in the Balearic Basin under summer and winter conditions, and for two waveforms (8 s CW and 10 Hz LFM) received at the broadside beam; use was made of the bottom backscattering values shown at Fig. 28.

5.5. LONG-RANGE BACKSCATTERING

Long-range returns are dominated by directional returns from highlights of the seafloor, such as seamounts, sea pinnacles and islands, coastlines and continental shelves. This dominance is seen in the real-time colour displays of Sect. 4, where the Sardinian and Corsican shelves stand out clearly for measurements made in the Balearic Basin, and for measurements in the Tyrrhenian Sea, where the island of Ustica, the Pliny and Vavilov seamounts, and the Sicilian and Neapolitan coasts provide large returns. The directionality is more visible with LFM waveforms, which have high range resolution capability, but is equally valid for CW signals. Estimates of the equivalent target strength of the major bathymetrical features can be as high as 60 dB.

Good correlation for the major features is found between the LFM and CW returns, with the latter all centered at zero doppler shift, indicating that they are

attributable to stationary targets. All doppler-shifted returns discernible in the CW displays can easily be associated with major features in other directions. Since these returns are picked up through the sidelobes, the beamformed output is not only attenuated but also frequency shifted, as discussed in Subsect. 2.4. Large features, with a high equivalent target strength, generate echoes 50 dB or more above the ambient noise level, and since practical sidelobe rejection is no better than 30 dB, on beamforming these returns will affect any other beams with levels of 15 dB or more above ambient noise. All returns from major bathymetric features have a complex sidelobe structure, both in range (or time) and in frequency; this is most likely a consequence of the multipath associated with the long-range returns.

Figures 31 to 34 show various examples of the spectral time histories of returns from transmissions of an 8 s, 370 Hz signal, along beam directions with various major features such as seamounts and pinnacles (for examples the Pliny and Vavilov seamounts at Figs. 31 and 32 respectively), islands (Ustica at Fig. 33) and coastlines or continental shelves (western coast of Corsica at Fig. 34). These figures are plots of the bathymetry along the beam pointing direction, all with a common range scale adjacent to the received spectral time history in order to illustrate the correlation between received intensities and bottom geometrical features (depth and sloping).

6. Statistical analysis of the received intensities

6.1. INTRODUCTION

The interest in a higher-order statistical analysis of the received intensities for an activated towed array is twofold: on the one hand it helps to gain a better insight into long-range propagation and scattering effects of importance in the sub-kilohertz region; on the other hand it provides a useful input to the evaluation of the performance of detection and parameter estimation algorithms suitable for the possible operational applications of the activated towed array concept.

Reverberation is a highly non-stationary process, and therefore the only strictly valid statistics are those that apply to ensemble averaging. However it is not always possible, for practical reasons, to collect large sets of independent sample transmissions (*pings*) for ensemble averaging. Indeed, in the experimental set-up the number of pings over which one estimates ensemble statistics is always small (a maximum of 30), and cannot be made much larger if homogeneity among data sets is to be preserved; the variation among data sets is due to the changing of the environment caused by the motion of the acquisition platform. Additionally, from the long-range sonar detection standpoint, decisions as to the presence or absence of targets must usually be made on the basis of small-sample sets. Therefore one first establishes the relationship between the small-sample sets and their ensemble statistics in order to derive the general properties of the medium and evaluate detection algorithms.

The analysis carried out so far has investigated the *amplitude statistics* of the received intensities after beamforming, matched filtering and envelope detection. It is therefore essentially a narrowband variance analysis. An example of the input is given at Figs. 35 and 36. The waveforms that have been analysed had relatively high range resolution (LFMs or short CWs) and yielded enough *independent time samples* for reliable higher-order statistics. Figure 35 shows a typical time history of the received intensities for one single ping and a LFM signal of 8 s duration and 10 Hz bandwidth (broadside and endfire beam data). Figure 36 presents the same data as Fig. 35, but all pings for the same run have been ensemble averaged. The smoothing effect is evident although the number of pings is limited (only 15). *Ensemble* linear averaging is applied by the combining and averaging of the magnitudes from different pings sampled at the same time instant relative to their individual transmission instants. The standard deviation of the intensities (expressed in dB) is related to the coefficient of variation of the linear averaging and is indicated in the lower half of each plot at Fig. 36, with the scale on the right-hand side. Since the tow vessel is moving during the run, features that are independent of actual

location will be properly averaged whereas those that are not independent, such as returns from objects whose relative geometry changes, will be smeared.

In Figs. 35 and 36 it is possible to distinguish three discrete regions dominated by three distinct processes. The first region, which extends up to about 40 km, is dominated by reverberation, in particular bottom reverberation as discussed in the previous sections. The second region, which extends beyond the first one up to about 90 km, is dominated by large returns from an extended target, here part of the Continental shelf off the western coast of Corsica. The third, beyond 90 km, appears to be dominated by ambient noise alone. This clear-cut separation made this kind of data set convenient for the present statistical analysis and has been used in the following sections to illustrate the method of application.

The methodology is based on the extensive use of non-parametric hypothesis testing, particularly in regard to stationarity and the distribution types of the received intensity time series, since these are the most relevant statistics for sonar detection. The advantage of using non-parametric statistics is that they are 'distribution-free', i.e. they do not need an underlying assumption (usually of normality) on the population. This is important when either the number of samples is small or when the data are by their nature non-normal or non-stationary, as is the case in reverberation-dominated processes. Note too that in order to apply the statistical tests it is necessary to operate on *independent* samples. Since the processed data base is oversampled, a decimation-in-time is required. Decimation by a factor of two usually gives enough de-correlation to provide the required independence between successive samples.

In the following section, non-parametric tests are introduced for the analysis of data limited by (stationary) ambient noise. Since reverberation-dominated stochastic processes can usually (with care) be reduced to stationary processes, as it will be shown later, the same statistical tools can be applied to the analysis of the fluctuations process obtained by the decomposition of the original process.

6.2. ANALYSIS OF AMBIENT NOISE LIMITED DATA

Although ambient noise intensities below 1 kHz are subject to long term variations and are significantly affected by the level of shipping noise, it is accepted that over limited time intervals (a few minutes) stationarity can usually be assumed, see for instance [29]. Examination of the data set under investigation (shown at Figs. 35 and 36) revealed it to be well behaved and accordingly provided a good basis as a reference for the application of the techniques. The good behaviour was attributed to there being no nearby or remote shipping affecting returns over all pings, and no contamination of beams by towship noise other than in the forward endfire beam.

The grand average of the intensities *received over those ranges dominated by ambient*

noise is consistent with that measured independently on a broader band with a single hydrophone, and is in good agreement with the Wenz/Knudsen curves for the wind and sea-state conditions at the time of the run. The average value is 46.8 dB re μPa (see Table 6), and by adding 25 dB for array and processing gain a noise level of 71.8 dB re μPa/Hz is obtained.

But the point of interest is the fact that in general the *ensemble average of the standard deviation of the dB averages over time*, is 5.56 dB. This result is in agrement with standard theories of long-range ocean acoustic propagation in a SOFAR-like channel (see Frisk [30]). Notably, Dyer's theory [31] shows that if scattering can be considered negligible with respect to propagation effects, multipath can be modelled as an incoherent superposition of many (although as few as 4 may work as well) random vectors of approximately identical energy associated with each path. On converting the received intensities to a logarithmic scale, therefore, their *dB mean* has a standard deviation with an expected value of 5.57 dB.

6.3. STATIONARITY TESTS

The indication that it is possible to interchange time and ping (or ensemble) averages for first-order statistics points to a form of a weak stationarity. This was tested by means of the Mann-Whitney U Test, which is generally regarded as one of the most powerful non-parametric tests for the case of two independent samples (Siegel [32]) and avoids many of the weaknesses of the Parametric t Test. It is used for testing whether two groups have been drawn from the same population, through checking on the population medians, which for skewed distributions is usually a more reliable indication than checking the mean.

In the application described here the Mann-Whitney U Test was used to determine whether the received intensities over the assumed noise-limited region, formed a locally stationary sequence on a single ping basis. Since in sonar detection the interest is in maintaining the properties over as small an interval as is feasible, the methodoly that was applied was to divide the total data set into smaller contiguous subsets and run the Mann-Whitney U Test on each group by taking each subset pair once in combination with all the others. As is well known, the procedure for a non-parametric test is based on standard hypothesis testing and requires the setting of a threshold ϱ (the significance level) against which results are compared in order to decide whether the hypothesis must be rejected or not. In the present case the hypothesis to be tested was the stationarity of the time series and various significance levels were tried out. However, results are given only for the customary 5% level, which was quite representative.

Selecting a significance level ϱ means that if the test can be run for many times on independent samples and the hypothesis is true, there should be approximately 100ϱ% rejections. In the stationarity tests the total number of independent data

per ping was fixed, and so a trade-off resulted between the subset (or record) size and the number of independent tests. Tests were then run for three record lengths on each ping. The results are shown in Table 4, where the percentage rejection obtained by running the tests at the 5% significance level is indicated. The results indicate that stationarity cannot be rejected. In fact, the selected testing criterion is rather restrictive in that it is equally affected by records which are close or that are widely separated in time. The test is quite sensitive even to relatively small variations of the rms intensity fluctuations, and therefore in the presence of reverberation or extended target returns the percentage rejection is very high.

6.4. PROBABILITY DISTRIBUTION ESTIMATION

Due to there not being enough samples for ensemble statistics probability densities and distributions have been estimated here only for independent *time samples*. However, when the time series is stationary these statistics are also the ensemble statistics. The evaluation of the distributions was also based on non-parametric statistical methods instead of the plotting of histograms or the tabling of percentiles. The method consisted of determining whether at a preset significance level a given, theoretical distribution fitted the data, or out of a number of distributions one fitted the data best. The Kolmogorov-Smirnov (KS) goodness of fit test [32] which was used for this purpose is considered well suited.

The theoretical densities that were taken into account for the received intensities (magnitude data) were

(i) The Rayleigh or 2-degrees-of-freedom χ^2 density (this is the negative exponential density if the data are expressed as power values, and is the density of the envelope of a zero-mean gaussian input sequence).

(ii) The log-normal density, which does not arise from physical considerations, but is consistent with letting the parameters of the sonar equation to be gaussian random variables.

(iii) The Weibull density, Ref. [33], which is a two-parameter distribution that is sometimes used to describe radar land clutter. It is a distribution that can be made to fit either a Rayleigh or a log-normal density or, heuristically, distributions in between.

Other distributions can be considered, such as that arising from the gamma density and, notably, the Rice distribution which possibly is the most complete if associated with forms of coherent scattering or dominating path. However the Rice distribution is pretty unwieldy and (Urick [34]) it requires the estimate of an extra parameter, which ruled it out for this study.

The criterion in the application of the KS test is the same as the general one used in

TABLE 4

Results of the Mann-Whitney U test for stationarity

Stationarity (Mann-Whitney U) tests
Day: 6 Sept 85 - Signal: M1 - Broadside Beam
Range min 89.96 Range max 156.26

110 data/record 4 records 6 MW U tests

Ping #	% rejection (5% level)
1	0.00
2	0.00
3	0.00
4	33.33
5	16.67
6	0.00
7	0.00
8	0.00
9	0.00
10	0.00
11	16.67
12	0.00
13	0.00
14	50.00
15	0.00

avrg % rejection at 5% level = 7.78

55 data/record 8 records 28 MW U tests

Ping #	% rejection (5% level)
1	3.57
2	7.14
3	3.57
4	7.14
5	14.29
6	0.00
7	0.00
8	0.00
9	0.00
10	0.00
11	0.00
12	3.57
13	17.86
14	7.14
15	0.00

avrg % rejection at 5% level = 4.29

36 data/record 12 records 66 MW U tests

Ping #	% rejection (5% level)
1	7.58
2	0.00
3	1.52
4	4.55
5	6.06
6	1.52
7	4.55
8	0.00
9	4.55
10	0.00
11	7.58
12	6.06
13	10.61
14	12.12
15	6.06

avrg % rejection at 5% level = 4.85

the non-parametric tests, namely whether a set of independent samples comes from a specified theoretical distribution. The KS test determines the maximum difference (D) between the theoretical and the experimental cumulative distributions. The sampling distribution of D is known under the hypothesis of acceptance, and thus the estimated value can then be compared with a threshold to determine whether to reject the hypothesis at a specified significance level.

The test can be applied on each ping for a single set of all the available independent data points. The results for the data set presented in Table 4 are given along with first and second order statistics at Table 5. The rms intensities are definitely Rayleigh distributed, with an average standard deviation of the dB mean of 5.56 dB. This result has a general vlaidity. Tests performed on different beams and runs show that if the set passes the stationarity test then the data obey Rayleigh statistics. Note also that such tests are only really applicable to single-ping data: the ensemble averaged results at Fig. 36 (only data points beyond 90 km) have a very small variance (i.e. have a dominant deterministic component), and thus the test loses significance.

The experimental set of stationary, noise-limited data is plotted in Fig. 37a as a function of the normalized amplitude; Fig. 37b shows the corresponding cumulative distribution function versus the three theoretical distributions introduced previously. The horizontal axis in the figure is the amplitude normalized to the *experimental median*, and expressed in dB to facilitate comparison with the other curves; and the vertical axis is the quantity $1 - P(x)$, in log scale, where $P(x)$ is the cumulative distribution function. This rendition allows a readier appreciation of the behaviour of the experimental data *at the tails of the distribution*, where deviations from theoretical have a stronger effect on the probability of false alarm. An optimum linear processor is designed to operate with Rayleigh-distributed envelopes and therefore higher tails (such as those associated with a log-normal distribution) cause higher false alarm rates, and thus worse performance. In the present instance it can be seen that the data closely obey Rayleigh statistics. This being the case, the Weibull distribution essentially overlaps the Rayleigh distribution.

6.5. REVERBERATION STATISTICS

When the process includes some form of scattering or has varying *rms* levels, its statistics are highly non-stationary and the distributions depart from the Rayleigh model and tend towards a log-normal or Weibull distribution.

Figure 38b for instance, repeats the cumulative distribution function versus normalized logarithmic amplitude for the data set shown in Fig. 38a—which is dominated by reverberation returns (intensities received over the first 40 km of range). The large departure from the theoretical Rayleigh model, and the agreement over the tails with a Weibull model close to the log-normal case, are readily evident. Inte-

TABLE 5

Kolmogorov-Smirnov test and statistics on noise limited data

```
   Day: 6 Sept 1985 - Signal: M1 - Broadside Beam
  Range min =   89.96 km,   Range max =  156.26 km
  K - S test of prob density type =  Rayleigh
  on  442 samples per ping

          Ping #      1
dB Mean & std     =        46.4            5.69
Linear mean & std =        251.            143.
Passed K-S Test at  2% significance ?? YE
Passed K-S Test at  5% significance ?? YE
Passed K-S Test at 10% significance ?? NO

          Ping #      2
dB Mean & std     =        46.9            5.60
Linear mean & std =        264.            138.
Passed K-S Test at  2% significance ?? YE
Passed K-S Test at  5% significance ?? YE
Passed K-S Test at 10% significance ?? YE

          Ping #      3
dB Mean & std     =        46.2            5.91
Linear mean & std =        245.            130.
Passed K-S Test at  2% significance ?? YE
Passed K-S Test at  5% significance ?? YE
Passed K-S Test at 10% significance ?? YE
                      .
                      .
                      .
                      .

          Ping #     13
dB Mean & std     =        46.6            5.60
Linear mean & std =        255.            139.
Passed K-S Test at  2% significance ?? YE
Passed K-S Test at  5% significance ?? YE
Passed K-S Test at 10% significance ?? YE

          Ping #     14
dB Mean & std     =        47.3            5.32
Linear mean & std =        271.            134.
Passed K-S Test at  2% significance ?? YE
Passed K-S Test at  5% significance ?? YE
Passed K-S Test at 10% significance ?? YE

          Ping #     15
dB Mean & std     =        46.6            5.15
Linear mean & std =        248.            125.
Passed K-S Test at  2% significance ?? YE
Passed K-S Test at  5% significance ?? YE
Passed K-S Test at 10% significance ?? YE

K - S TEST GLOBAL STATISTICS on   15 pings
avrg dB mean  =   46.8      its std =  0.357
avrg lin mean =   259.      its std =   11.0
avrg dB std =   5.56
% rejection at  2% level =  0.00
% rejection at  5% level =  0.00
% rejection at 10% level =  6.67
```

restingly, although the Weibull distribution fits the data better at the higher tails, the KS test actually indicates that the data adhere more closely to log-normal statistics. This is because the test considers all data points, whereas the (distorted) image expands a relatively small but important percentage of data.

Following the approach of Ol'shevskii [6], and Plemons, Shooter and Middleton [35], the statistical properties of reverberation can be analysed even in the absence of experimental ensembles, by investigating the reverberation time covariance and, in particular, reducing the process to a (weak) stationary one wherever possible.

The covariance of a stochastic process $s(t)$, is given by

$$C_s(t_1, t_2) = E\langle s(t_1)s(t_2)\rangle , \tag{29}$$

where $E\langle \ldots \rangle$ denotes ensemble averaging. For a weakly stationary process C_s is a function only of $\tau = t_1 - t_2$. If the stochastic process $s(t)$ can be represented by the product of two independent functions

$$s(t) = r(t)q(t) \tag{30}$$

with $r(t)$ a rapidly fluctuating, stationary process, with covariance $C_r(\tau)$, and $q(t)$ a deterministic function representing the trend or slow rms variation, it follows that

$$C_s(t_1, t_2) = q(t_1)q(t_2)C_r(\tau). \tag{31}$$

And then if the function $q(t)$ varies slowly over the averaging interval (which occurs when $q(t_1) \simeq q(t_2)$)— the covariance $s(t)$ is a process reduceable to stationarity, and the decomposition at Eq. (30) is applicable, and the statistical properties can then be derived by time averages. The *local covariance stationarity* therefore implies the following:

(i) The geometries, and beam patterns of the experiment, as well as the scattering mechanisms vary slowly over the time intervals of averaging.

(ii) The averaging time windows must be appropriately chosen.

If reverberation can be assumed to be locally stationary, then a technique known as logarithmic normalization (van Schooneveld [36]) can be applied to decompose the time series into a rapidly fluctuating and stationary process and a slowly varying function called the *trend*, which represents the deterministic contributions of the scattering experiment. By taking the log of $S(t)$ as expressed by Eq. (30) it is

$$S(t) = R(t) + Q(t) , \tag{32}$$

where

$$S(t) = 10 \log s(t) ,$$
$$R(t) = 10 \log r(t) ,$$
$$Q(t) = 10 \log q(t) .$$

The logarithmic conversion transforms the normalization into a linear operation and can then be handled through linear filtering methods, such as Fast Fourier Transform algorithms.

Theoretically an analytic description of the deterministic component, such as the correlation structure or its spectrum, should be available. By subtracting the spectrum from the frequency representation of the original process it should then be possible to derive the properties of the stationary component. This is seldom feasible in practice; however, it is important to note that for Eq. (30) to hold there must be an appreciable difference between the correlation characteristics, and thus between the *spectral behaviour* of the two processes (conditions (i) and (ii)). Therefore although the analytic structure of $Q(t)$ may not be known, it must however be confined to the low-frequency part of the spectrum; in other words it must be a *slowly varying* process. If that is the case, a sub-optimum technique which is simple yet quite robust can be used: it involves choosing a threshold ω_0 by an iterative process which leads to the high-frequency part of the spectrum passing stationarity tests. Having set such a threshold, it is then possible to apply ideal filtering by removing (through setting to zero) either the low or the high portion of the spectrum. The result is a simplified representation of the type

$$\mathcal{F}S(\omega) = \mathcal{F}R(\omega) + \mathcal{F}Q(\omega)\,, \tag{33}$$

where the prefix $\mathcal{F}$ represents the power spectrum, with

$$\mathcal{F}R(\omega < \omega_0) = 0\,,$$

and

$$\mathcal{F}Q(\omega > \omega_0) = 0\,. \tag{34}$$

In other words, instead of looking for the optimum transfer function to decompose the process, a simpler spectrum truncation is applied. Note that this is a batch processing technique, since it requires having the whole time series available.

The power spectra of two typical sequences of received log intensities, one dominated by reverberation and the other dominated by ambient noise, are shown in Fig. 39. Figure 39a is related to the data at Fig. 37a, and Fig. 39b is related to the data at Fig. 38. The frequency range of the transform is based on the data sample rate, here 5 Hz for 0.1 s data rate. The Fourier transform is applied by means of the FFT algorithm, and therefore the discontinuities at the edges of the sample introduce some noise into the high-frequency part of the spectrum. When the process is stationary the spectrum shows no relevant peaks or slopes. When, on the contrary, data include trend variations or regular patterns coming from gross features, the power spectrum shows the presence of slopes and peaks that

affect the low-frequency region. It is in general visually easy to distinguish between low- and high-frequency components coming from slow and rapidly varying effects respectively.

By taking the inverse Fourier transform it is thus possible to extract both the trend and a process that represents the rapid fluctuation around the trend. In the log scale this last process is, by definition, a zero mean process; its statistics are of interest to the sonar detection case. The linear process, which has a normalized mean, was again tested with the KS test of goodness of fit to determine the applicable distribution type. The general result is that even in the presence of strong reverberation a well chosen cutoff frequency yields data with a strong tendency to be Rayleigh distributed. Note that since the Rayleigh distribution is a single parameter distribution, and since for the normalized process the median is unity by definition, the variance is constrained. An example of the fluctuations process obtained by removing the trend from the data at Fig. 38 is shown in Fig. 40, which also presents the cumulative distribution, and this is seen to closely fit the Rayleigh model.

7. Conclusions

This report summarizes results of reverberation measurements made with a low-frequency activated towed array and the findings of a preliminary analysis of the data collected.

The experimental data pertaining to the reverberation observed when operating in the Mediterranean Sea and in the middle of the sound channel, at moderately high power, has been interpreted and provides the following conclusions:

(a) Volume reverberation is not significant for the frequencies and experimental set-up utilized in this locality.

(b) Surface scattering was lower than predicted by the standard models, and was always overshadowed by bottom scattering.

(c) Bottom reflections in the vertical water column (the fathometer returns) and bottom backscattering dominated the received intensity time series.

(d) Agreement with model predictions was generally good whenever the model input parameters for the systemat-related and environmental conditions were accurately known.

(e) Bottom scattering strength was reasonably independent of frequency. Spectra with little or no doppler shift and spread were observed, but with high tails in the sidelobes. Long-range returns (beyond about 20 n.mi) was usually dominated by directional returns from extended targets such as seamounts and pinnacles, bottom slopes and continental shelves, islands and coastlines.

A statistical analysis was made of the received intensities generated by transmitting frequency modulated and relatively short (1 s) continuous wave signals. Higher-order statistics were investigated by extensive use of non-parametric hypothesis testing. In general, it turns out that returns dominated by ambient noise, if not contaminated by towship or nearby shipping noise, were usually stationary and adhered to Rayleigh statistics to various levels of confidence. Received time series dominated by reverberation are always highly non stationary, with log-normal or Weibull amplitude statistics *in time*, however reverberation can be assumed to be locally covariance stationary. By applying logarithmic normalization techniques it is thus possible to separate a slowly varying, non-stationary mean from a rapidly-fluctuating and mostly stationary series which in general obeys Rayleigh statistics.

References

[1] ANGRISANO, G. and SEGRE, A.G. La carta batimetrica del Mediterraneo nord occidentale, I.I. 1501. Genova, Istituto Idrografico della Marina Italiana, 1969.

[2] KERMABON, A., GEHIN, C. and BLAVIER, P. Numerical results of the analysis of sea-bottom cores, Volume I: Naples and Ajaccio Zones. SACLANTCEN M-46. La Spezia, Italy, SACLANT ASW Research Centre, 1968.

[3] BOVIO, E., JESPERS, S., MARANDINO, D., MARCHMENT, J., TOMPKINS, R. and WALSH, C. Summary report on Project 20 studies, SACLANTCEN SR-120 (to be published).

[4] KNIGHT, W.C., PRIDHAM, R.G. and KAY, S.M. Digital signal processing for sonar. *Proceedings of the IEEE*, **69**, 1981: 1451-1506.

[5] HARRIS, F.J. On the use of windows for harmonic analysis with the discrete Fourier Transform. *Proceedings of the IEEE*, **66**, 1978: 51-83.

[6] OL'SHEVSKII, V.V. Characteristics of Sea Reverberation. Consultants Bureau, New York, NY, Plenum, 1967.

[7] FAURE, P. Theoretical model of reverberation noise. *Journal of the Acoustical Society of America*, **36**, 1964: 259-266.

[8] MIDDLETON, D. A statistical theory of reverberation and similar first-order scattered fields. *IEEE Transactions on Information Theory*, Parts I and II: **13**, 1967: 372-414. Parts III and IV: **18**, 1972: 35-67.

[9] WEINBERG, H. Generic sonar model. NUSC TD 5971C. New London CT, Naval Underwater Systems Center, 1981.

[10] HOFFMAN, D.W. LIRA: A model for predicting the performance of low-frequency active-sonar systems for intermediate surveillance ranges, NOSC TD 259. San Diego, CA, Naval Ocean Systems Center, 1979.

[11] FRANCHI, E.R., GRIFFIN, J.M. and KING, B.J. NRL reverberation model: a computer program for the prediction and analysis of medium- to long-range boundary reverberation, NRL Report 8721, Washington, D.C., Naval Research Laboratory, 1984.

[12] WEINBERG, H. Navy interim surface ship model (NISSM) II, NUSC TR 4527. New London, CT, Naval Underwater Systems Center, 1973.

[13] URICK, R.J. Principles of Underwater Sound. 2nd edition. New York, NY, McGraw-Hill, 1975.

[14] DOUTT, J.A. Broadband measurements of volume scattering strength in the Mediterranean. SACLANTCEN SR-17. La Spezia, Italy, SACLANT ASW Research Centre, 1977.

[15] FORTUIN, L. Survey of literature on reflection and scattering of sound waves at the sea surface. *Journal of the Acoustical Society of America*, **47**, 1970: 1209-1228.

[16] STRUTT, J.W. *Lord Rayleigh*. The Theory of Sound. New York, NY, Dover, 1945.

[17] MARSH, H.W. Sound reflection and scattering from the sea surface. *Journal of the Acoustical Society of America*, **35**, 1963: 240–244.

[18] MARSH, H.W. SCHULKIN, M. and KNEALE, S.G. Scattering of underwater sound by the sea surface. *Journal of the Acoustical Society of America*, **33**, 1961: 334–340.

[19] ECKART, C. The scattering of sound from the sea surface. *Journal of the Acoustical Society of America*, **25**, 1953: 566–570.

[20] BREKHOVSKIKH, L. and LYSANOV, Yu. Fundamentals of Ocean Acoustics. Berlin, Springer, 1982.

[21] McDANIEL, S.T. Diffractive corrections to the high-frequency Kirchhoff approximation. *Journal of the Acoustical Society of America*, **79**, 1986: 952–957.

[22] CHAPMAN, R.P. and HARRIS, J.H. Surface backscattering strengths measured with explosive sound sources. *Journal of the Acoustical Society of America*, **34**, 1962: 1592–1597.

[23] CHAPMAN, R.P. and SCOTT, H.D. Surface backscattering strengths measured over an extended range of frequencies and grazing angles. *Journal of the Acoustical Society of America*, **36**, 1964: 1735–1737.

[24] SCHMIDT, P.B. Monostatic and bistatic backscattering measurements from the deep ocean bottom. *Journal of the Acoustical Society of America*, **50**, 1971: 326–331.

[25] RODERICK, W.I. and CRON, B.J. Frequency spectra of forward-scattered sound from the ocean surface. *Journal of the Acoustical Society of America*, **48**, 1970: 759–766.

[26] MARANDINO, D. and GOLDSBERRY, T.G. Evaluation of low-frequency bottom backscattering strength *vs* grazing angle by means of multiple beamforming. *In*: Akal, T. and Berkson, J.M. *eds*. Ocean Seismo-Acoustics, low-frequency underwater acoustics, proceedings of the Symposium organized by SACLANTCEN, held June 10–14, 1985, Lerici, Italy. New York, NY, Plenum, 1986: pp. 355–364.

[27] HASTRUP, O.F. and AKAL, T. Acoustic reflectivity measurements in the Mediterranean Sea, Volume 2. SACLANTCEN SR-28, NATO RESTRICTED. La Spezia, Italy, SACLANT ASW Research Centre, 1979. [AD C 950 692].

[28] BERKSON, J.M., AKAL, T., KLOOSTERMAN, H.J. and BERROU, J.-L. Directional measurements of low-frequency acoustic backscattering from the seafloor. *In*: Akal, T. and Berkson, J.M. *eds*. Ocean Seismo-Acoustics, low-frequency underwater acoustics, proceedings of the Symposium organized by SACLANTCEN, held June 10–14, 1985, Lerici, Italy. New York, NY, Plenum, 1986: pp. 327–333.

[29] JOBST, W.J. and ADAMS, S.L. Statistical analysis of ambient noise. *Journal of the Acoustical Society of America*, **62**, 1977: 63–71.

[30] FRISK, G.V. Intensity statistics for long-range acoustic propagation in the ocean. *Journal of the Acoustical Society of America*, **64**, 1978: 257–259.

[31] DYER, I. Statistics of sound propagation in the ocean. *Journal of the Acoustical Society of America*, **48**, 1970: 337–345.

[32] SIEGEL, S. Non-Parametric Statistics for the Behavioural Sciences. New York, NY, McGraw-Hill, 1956.

[33] SCHLEHER, D.C. Radar detection in Weibull clutter. *IEEE Transactions on Aerospace and Electronic Systems* **12**, 1976: 736-743.

[34] URICK, R.J. Models for the amplitude fluctuations of narrowband signals and noise in the sea. *Journal of the Acoustical Society of America*, **62**, 1977: 878-887.

[35] PLEMONS, T.D., SHOOTER, J.A. and MIDDLETON, D. Underwater acoustic scattering from lake surfaces. II. Covariance functions and related statistics. *Journal of the Acoustical Society of America*, **52**, 1972: 1503-1515.

[36] VAN SCHOONEVELD, C. Digital Logarithmic Normalization of Sonar Signals: Serial Processing. *In*: Griffiths, J. Stocklin, P. and van Schooneveld, C. *eds*. NATO A.S.I. Conference Proceedings, held at Loughborough, Academic Press, London, 1973

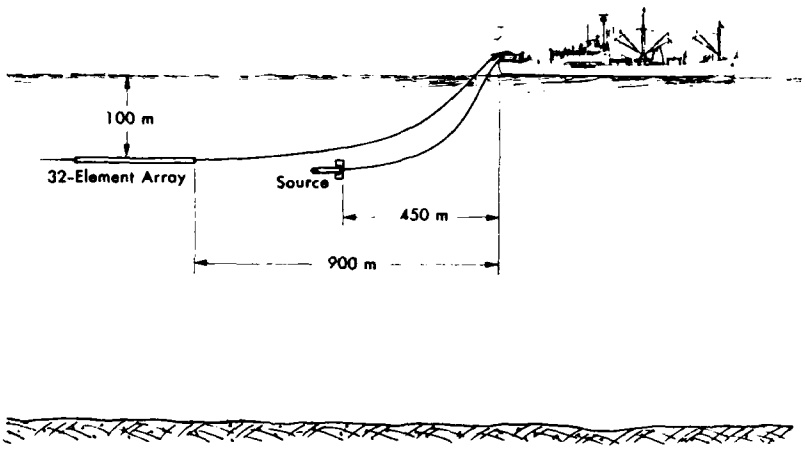

Fig. 1. Experimental set-up for reverberation measurements with an activated towed array.

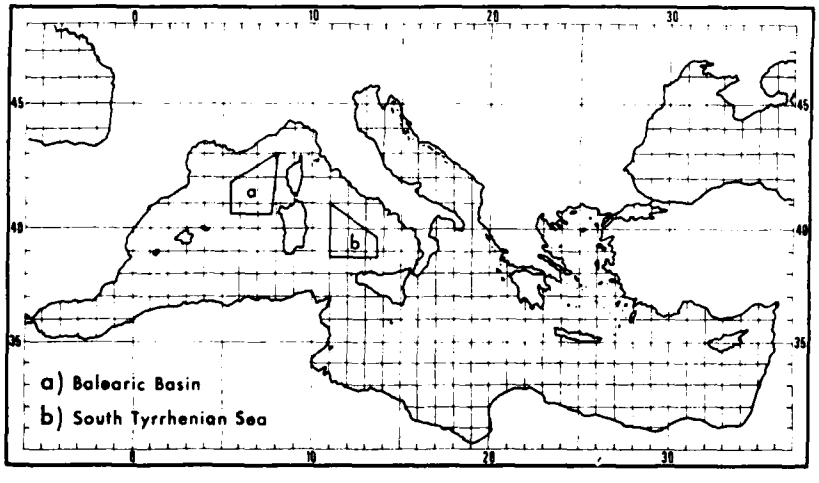

Fig. 2. Geographical areas of SACLANTCEN sea trials for deep-water reverberation measurements.

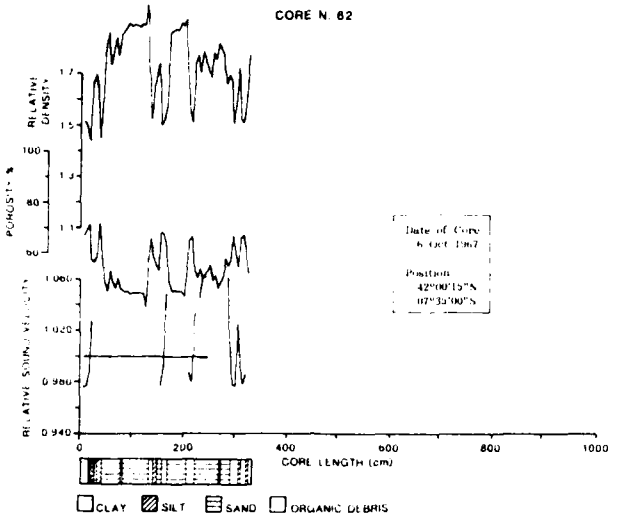

Fig. 3. Geophysical and acoustic parameters of a sample of seabed in the Balearic Basin (from [2]).

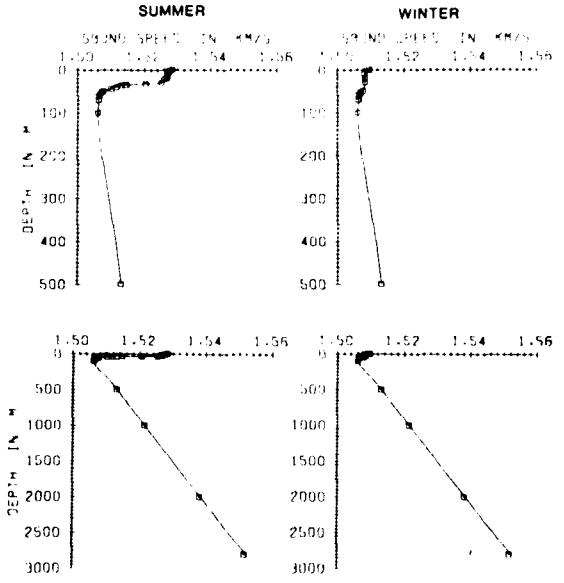

Fig. 4. Typical sound speed profiles (early April and early September data).

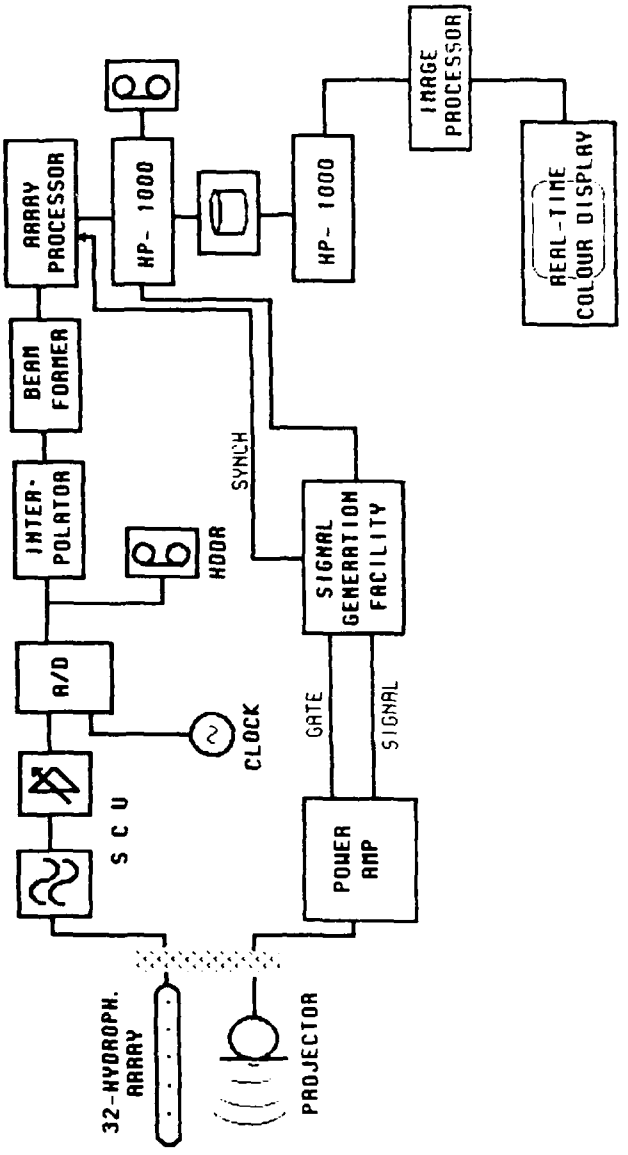

Fig. 5. Shipborne data-collection system; simplified block diagram.

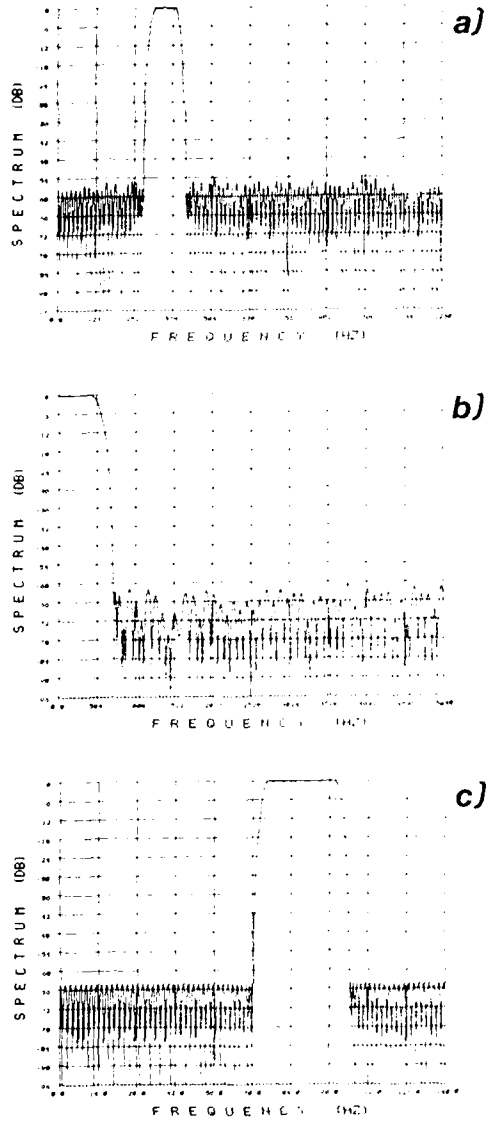

Fig. 6. Filter responses for 370 Hz acquisition: (a) first stage interpolator; (b) first anti-aliasing (interpolator); (c) second anti-aliasing (AP).

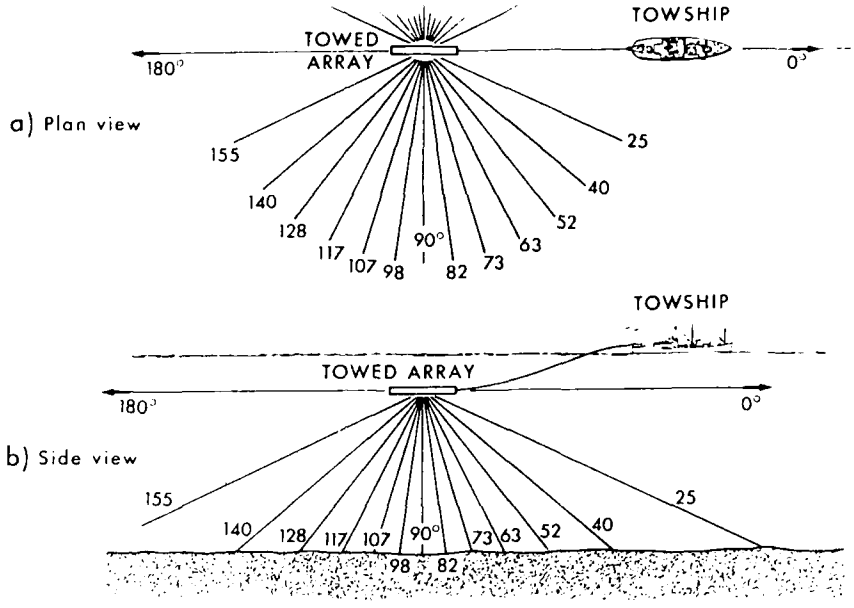

Fig. 7. Typical beams configuration (panoramic): (a) plan view; (b) elevation view.

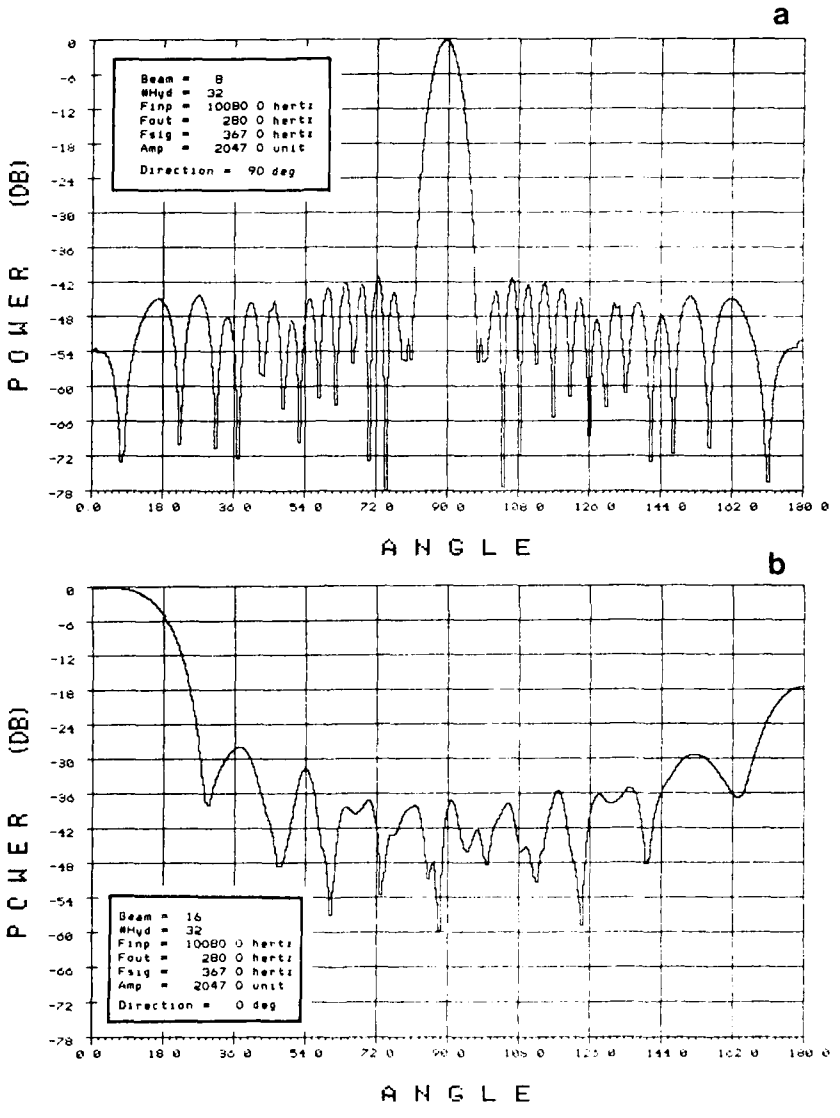

Fig. 8. Theoretical beam patterns at 370 Hz: (a) broadside beam; (b) endfire beam.

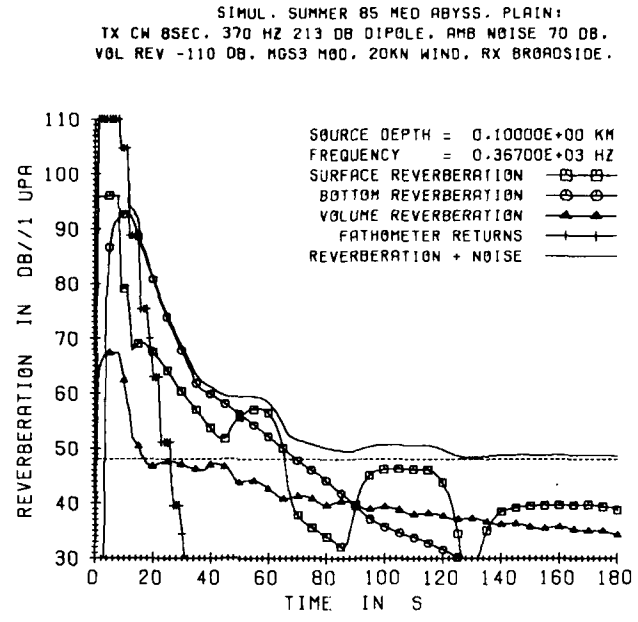

Fig. 9. GENERIC Sonar Model predictions (with default values) of reverberation at low-frequency, simulating this experimental set-up.

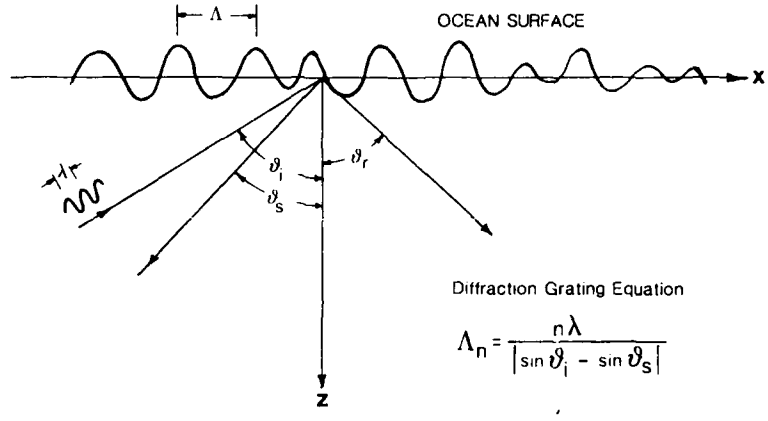

Fig. 10. Surface scattering geometry and the diffraction grating formula.

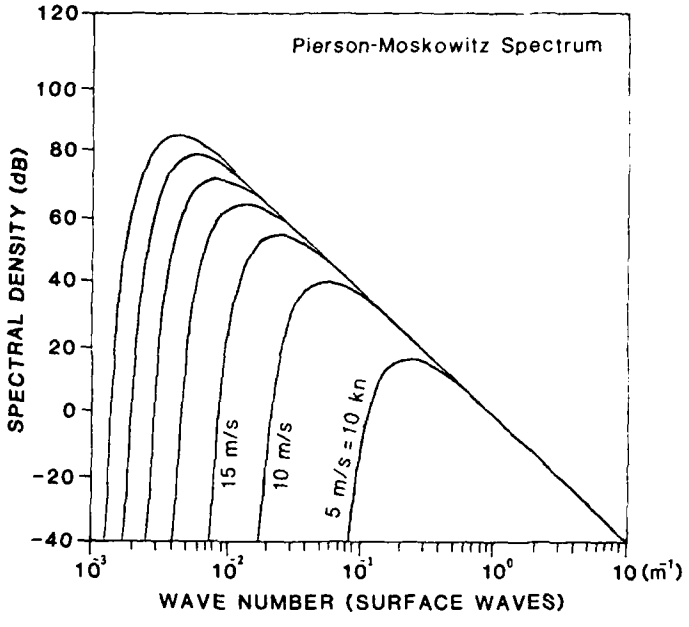

Fig. 11. Pierson-Moskowitz sea surface wave frequency spectrum.

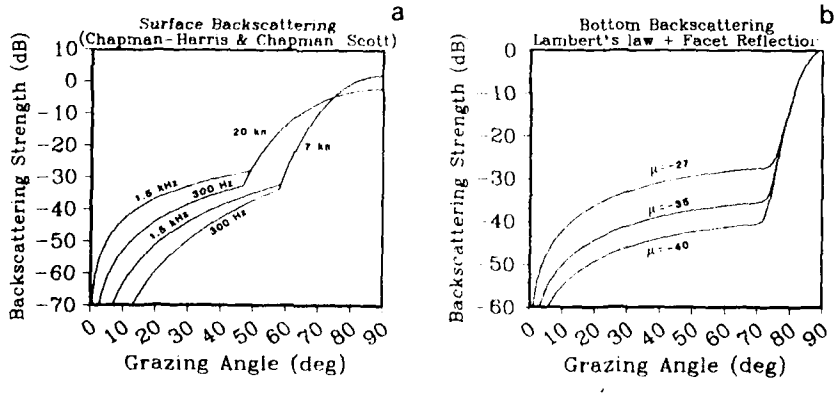

Fig. 12. Composite-roughness scattering: (a) surface backscattering strength (Chapman-Harris formula); (b) bottom backscattering strength (McKenzie formula)

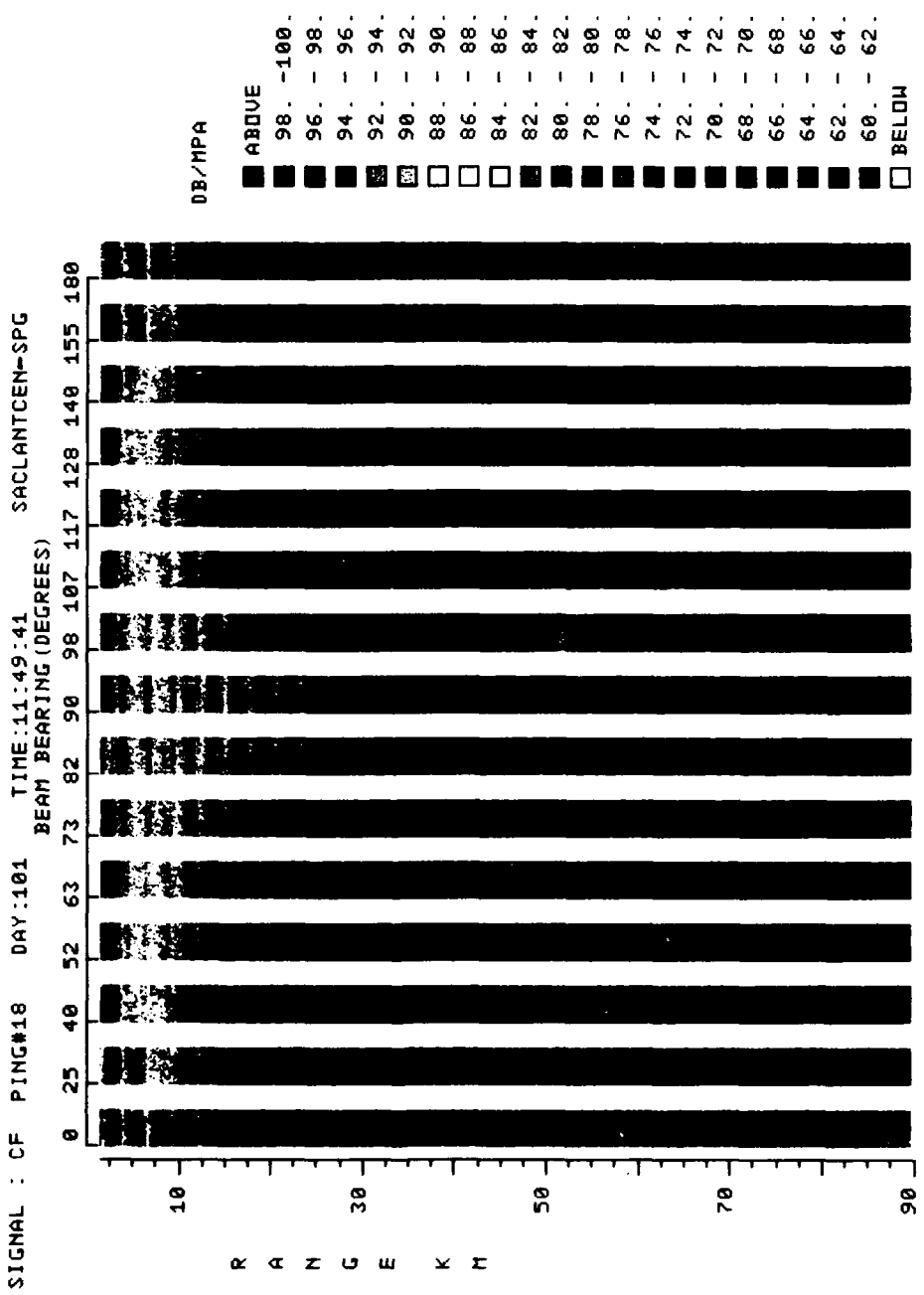

Fig. 13. Real-time multi-ping colour display of received, matched-filtered intensities as a function of beam and range (refer to text and Table 3): FM display only; signal CF, day 10, Apr. '84. Data in dB re μPa.

intentionally blank page

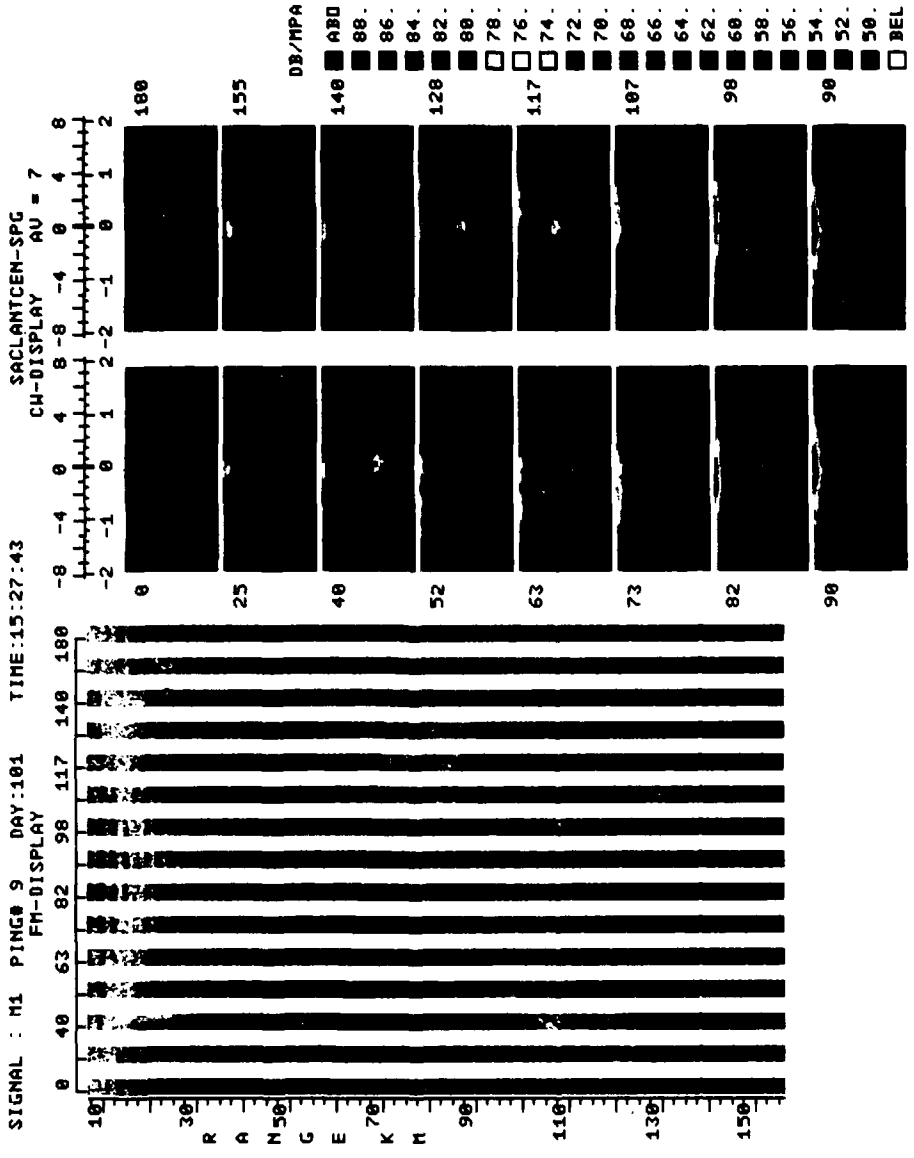

Fig. 14. Real-time multi-ping colour display of received, matched-filtered intensities as a function of beam, range and frequency (refer to text and Table 3): display of FM and CW data; signal M1; day 10, Apr. '84. Data in dB re μPa.

intentionally blank page

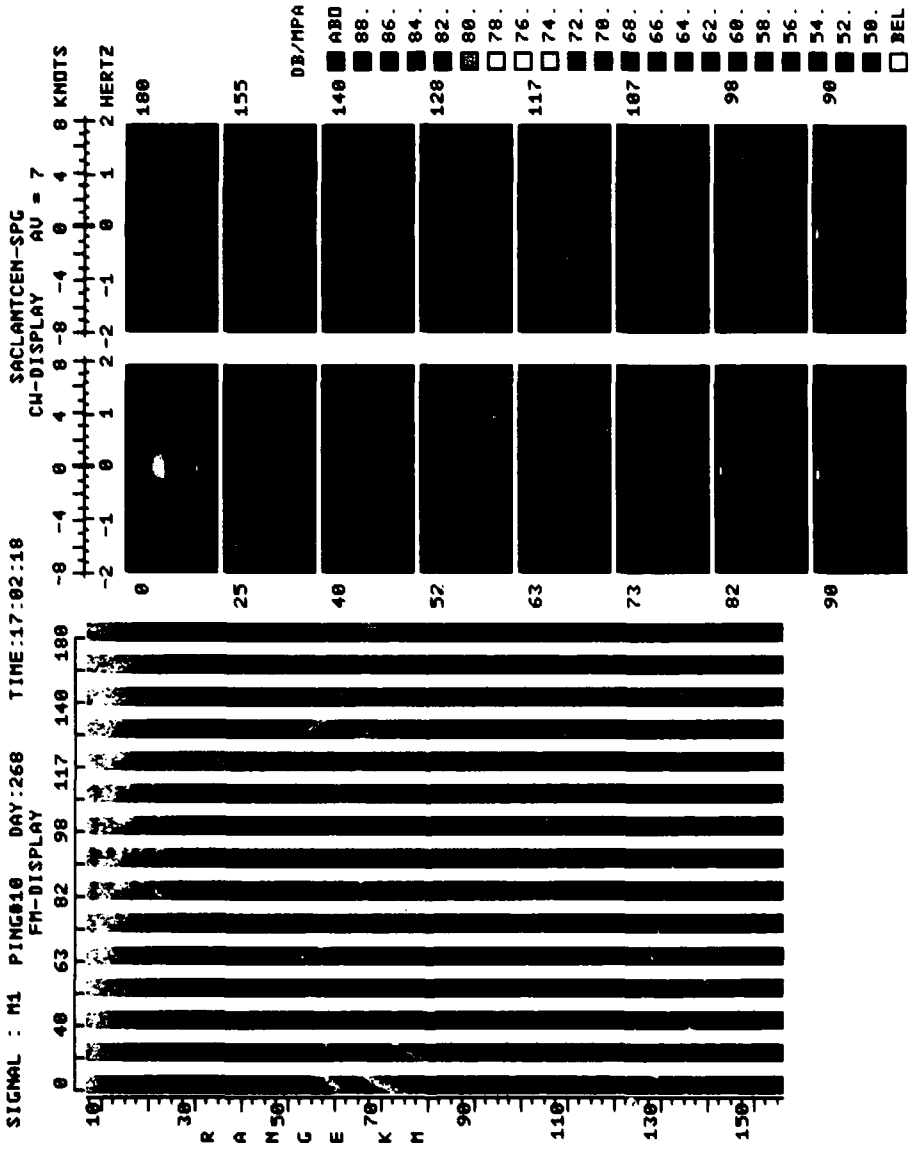

Fig. 15. Real-time multi-ping colour display of received, matched-filtered intensities as a function of beam, range and frequency (refer to text and Table 3): display of FM and CW data; signal M1; day 24, Sept. '84. Data in dB re μPa.

intentionally blank page

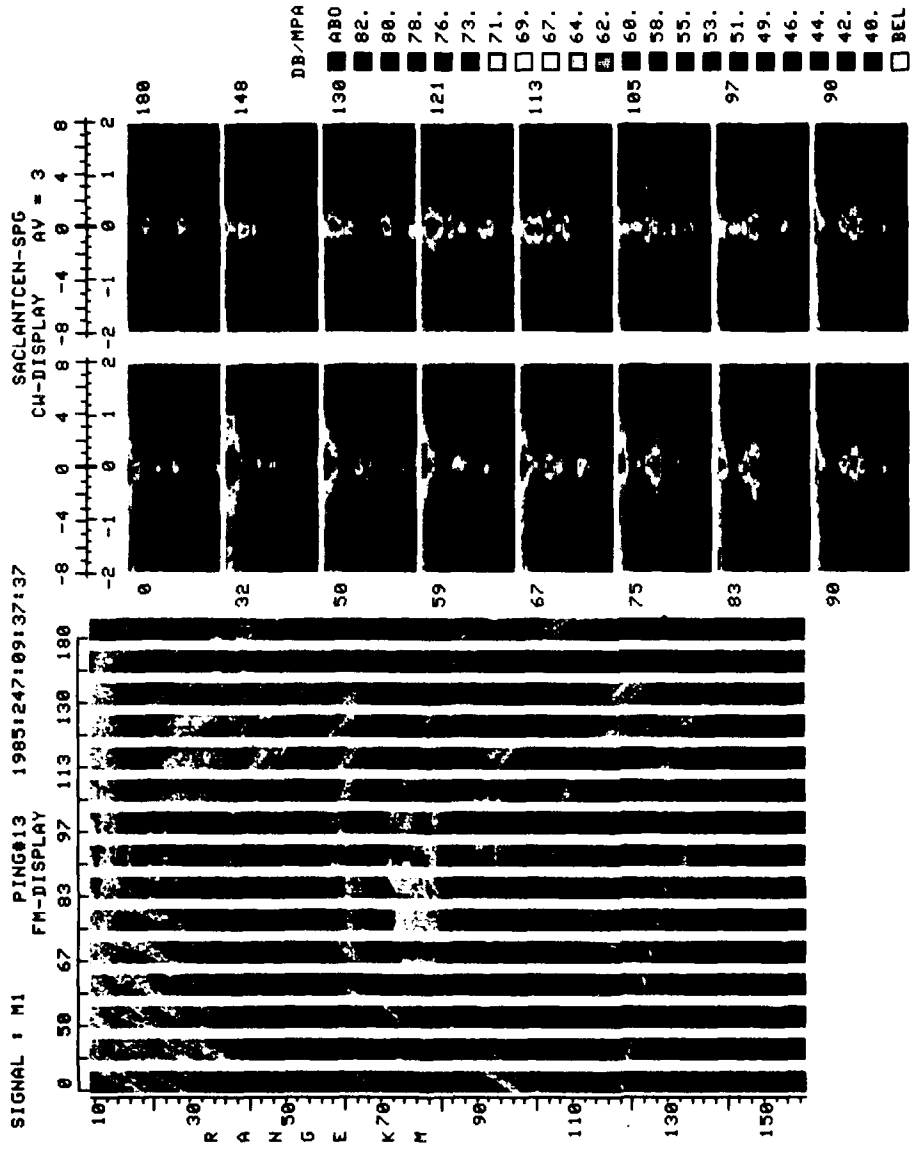

Fig. 16. Real-time multi-ping colour display of received, matched-filtered intensities as a function of beam, range and frequency (refer to text and Table 3): display of FM and CW data; signal M1, day 4, Sept. '85. Data in dB re μPa.

intentionally blank page

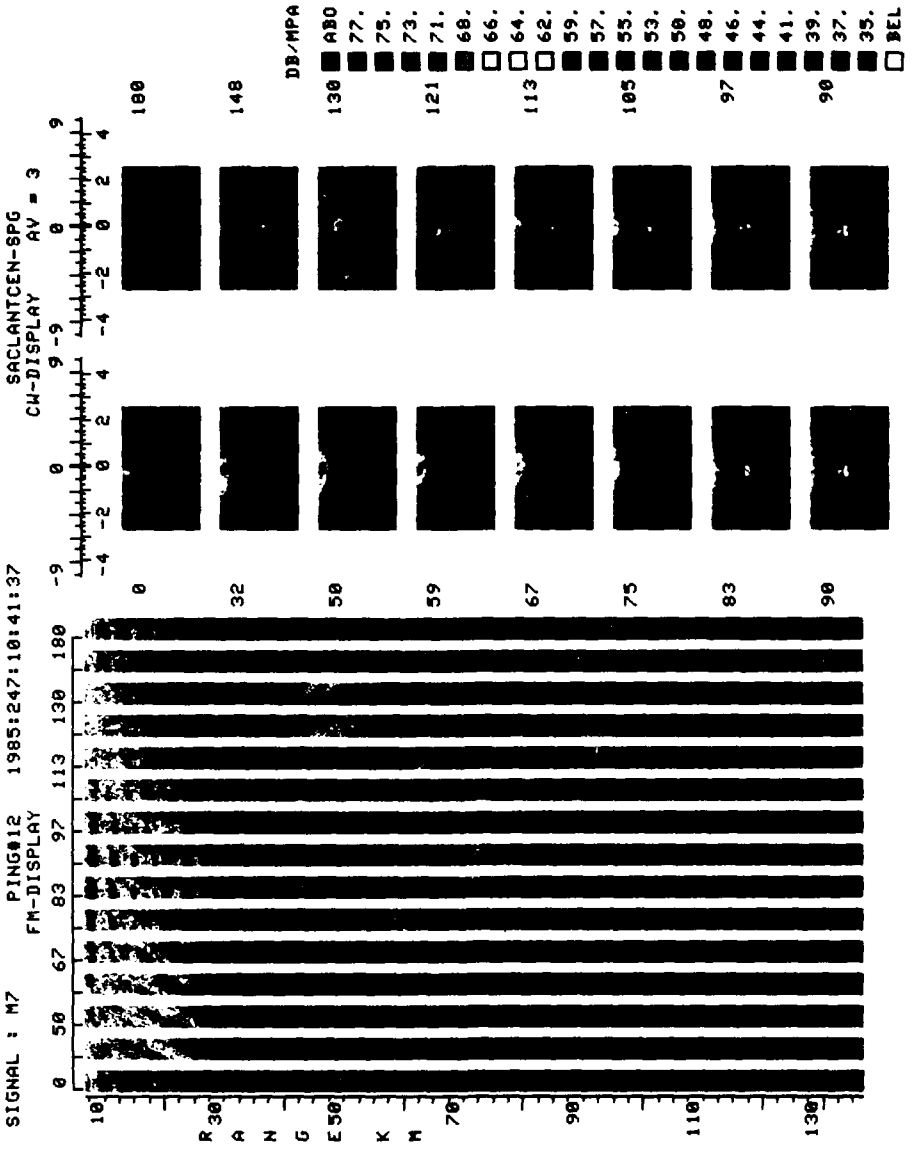

Fig. 17. Real-time multi-ping colour display of received, matched-filtered intensities as a function of beam, range and frequency (refer to text and Table 3): display of FM and CW data; signal M7; day 4, Sept. '85. Data in dB re μPa.

intentionally blank page

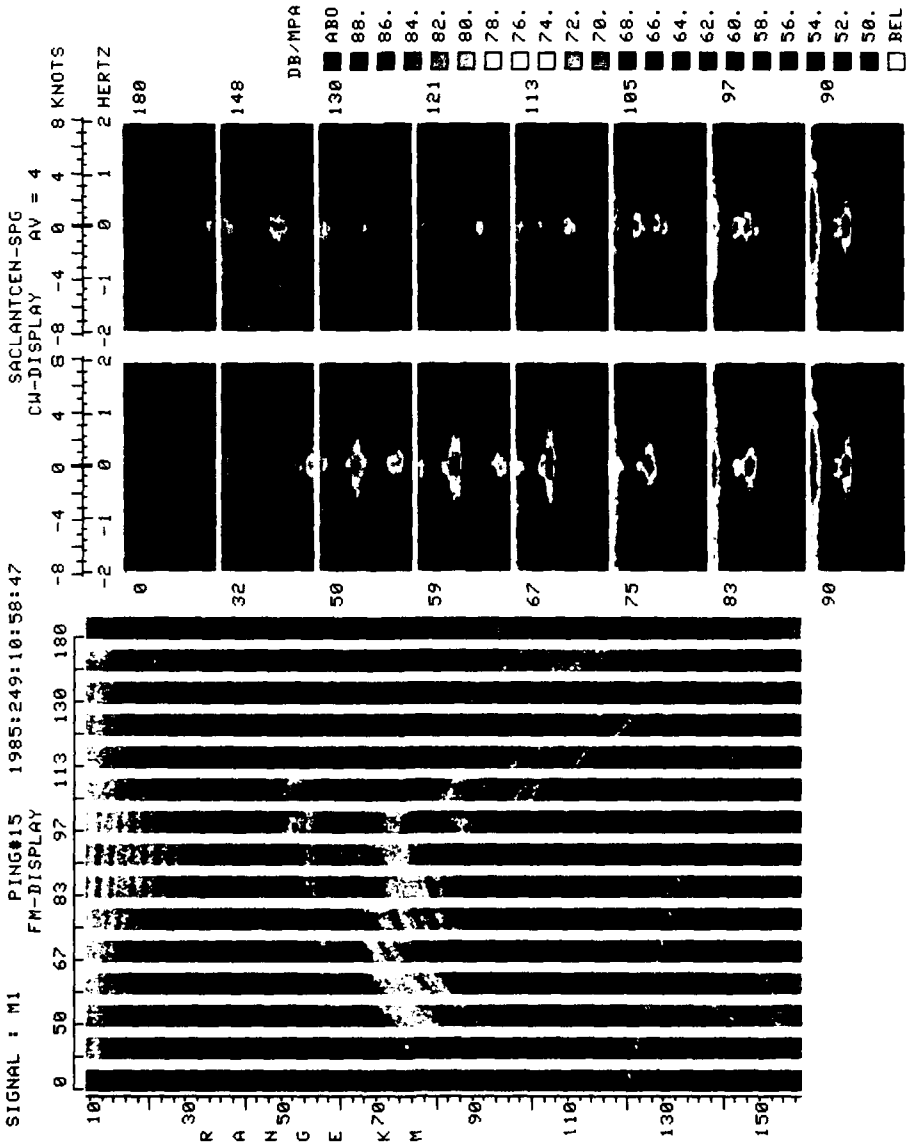

Fig. 18. Real-time multi-ping colour display of received, matched-filtered intensities as a function of beam, range and frequency (refer to text and Table 3): display of FM and CW data; signal M1; day 6, Sept. '85. Data in dB re μPa.

intentionally blank page

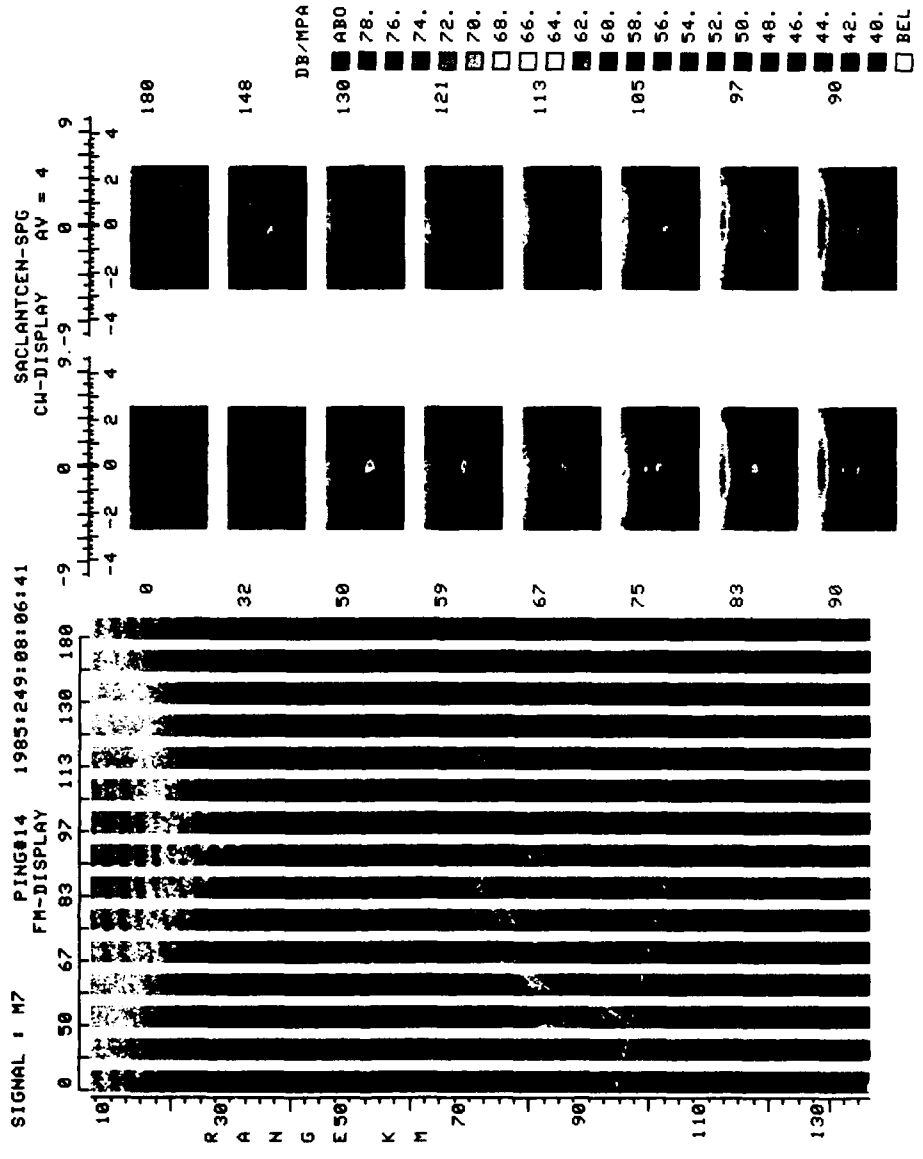

Fig. 19. Real-time multi-ping colour display of received, matched-filtered intensities as a function of beam, range and frequency (refer to text and Table 3): display of FM and CW data; signal M7; day 6, Sept. '85. Data in dB re μPa.

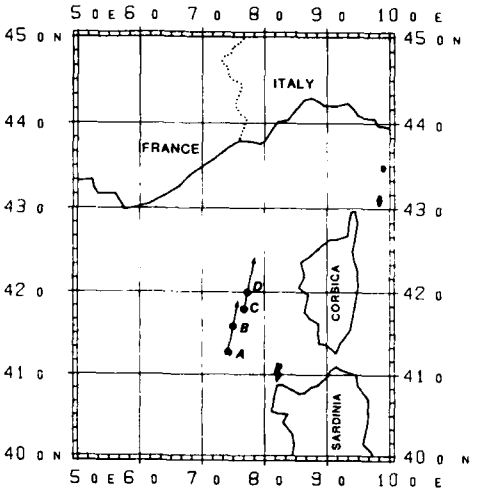

Fig. 20. Geographical locations and courses of the runs for the data at Figs. 13 to 19; refer to Table 3.

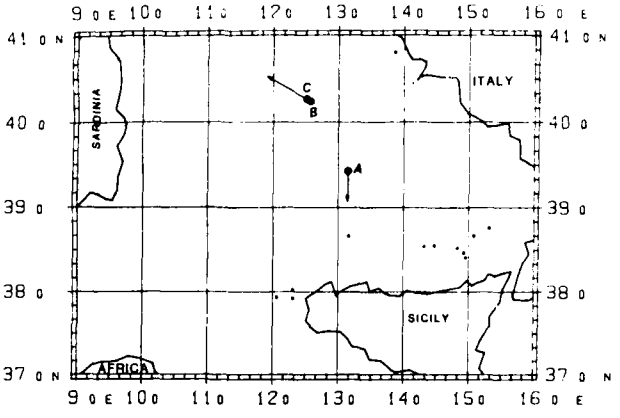

Fig. 21. Geographical locations and courses of the runs for the data at Figs. 13 to 19; refer to Table 3.

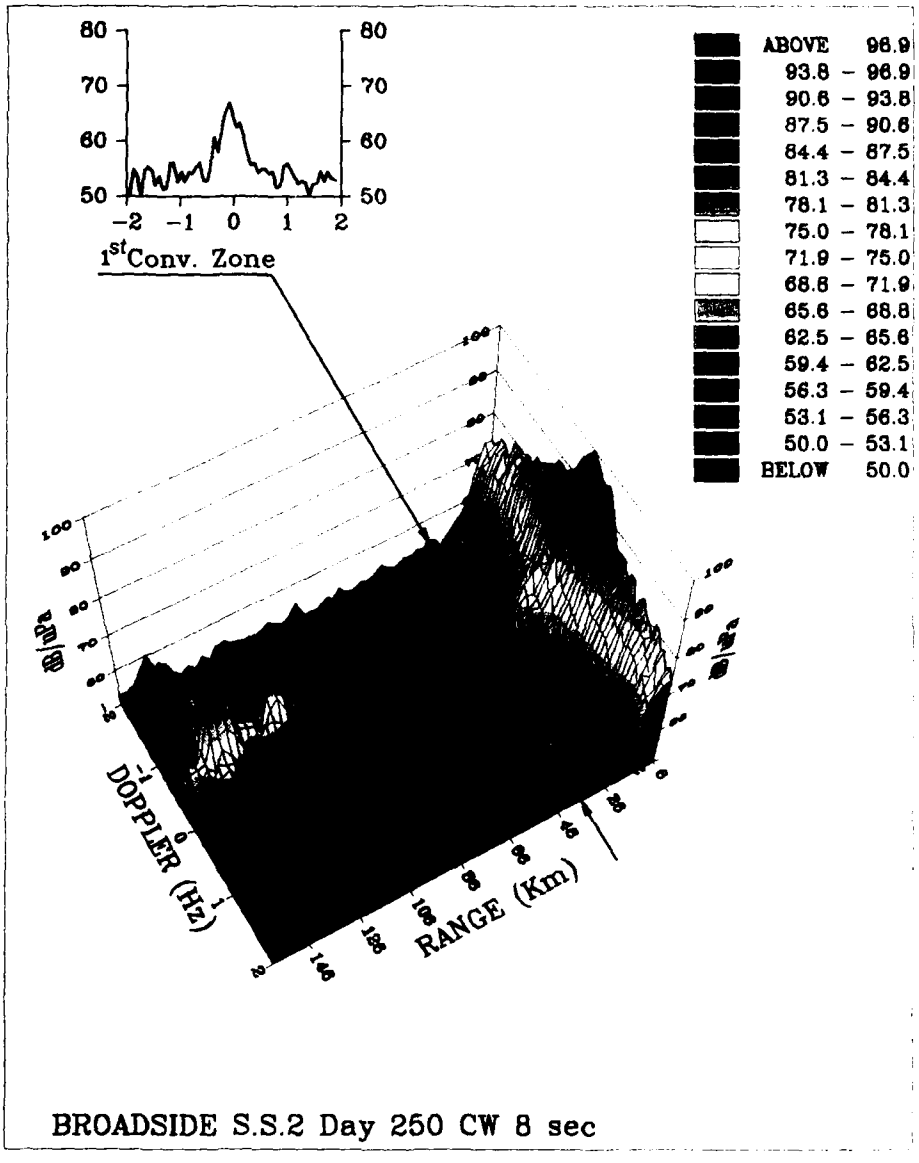

Fig. 22. Spectral time history of received intensities: 8 s, 370 Hz CW transmission; broadside beam; sea-state 2.

intentionally blank page

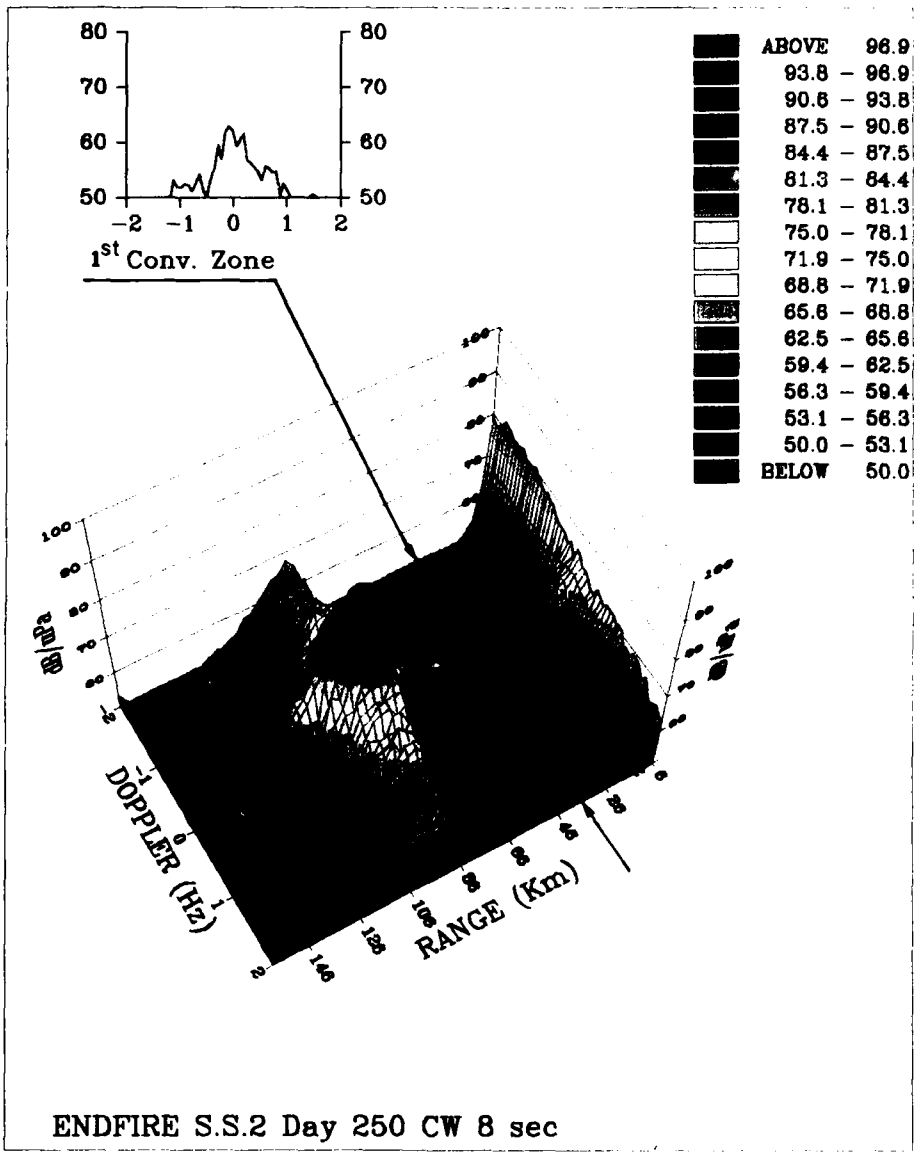

Fig. 23. Spectral time history of received intensities: 8 s, 370 Hz CW transmission; endfire beam; sea-state 2.

intentionally blank page

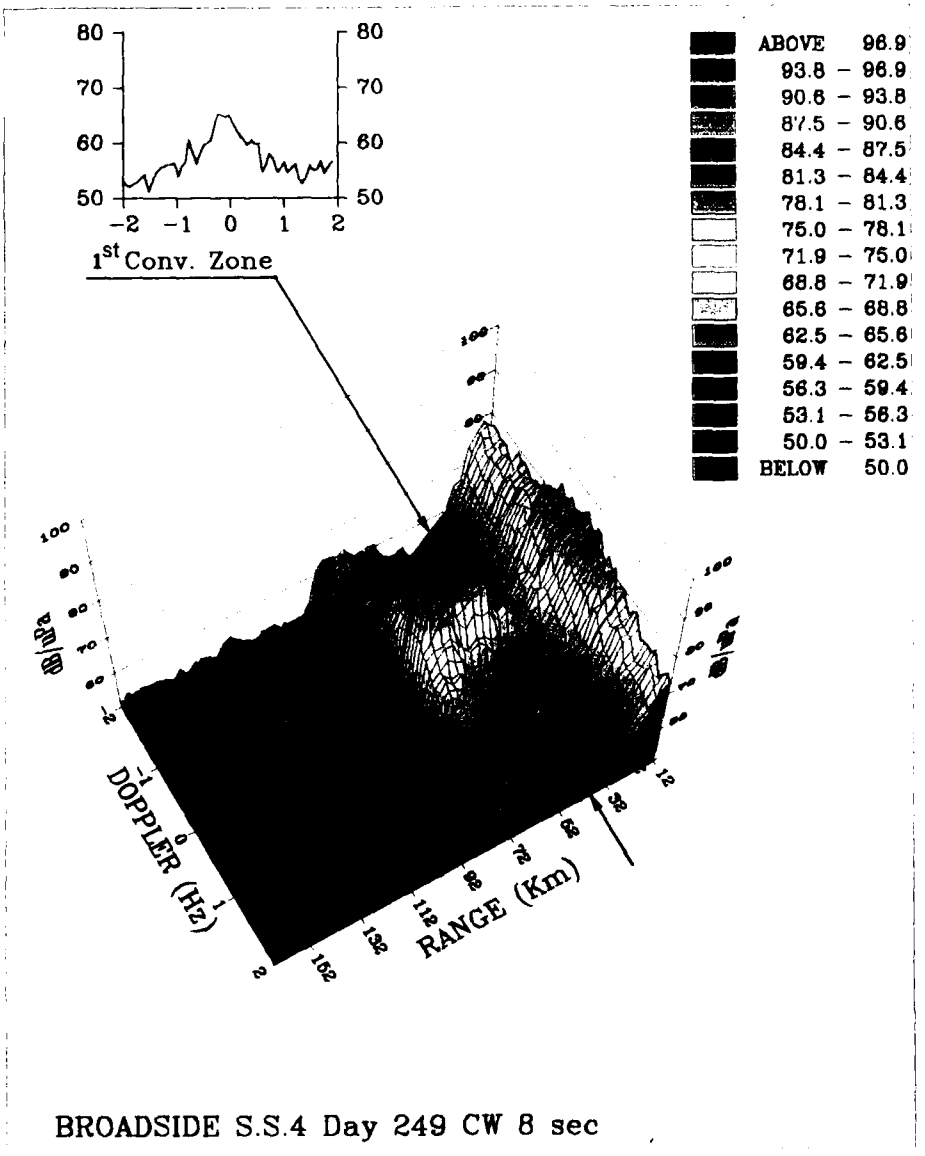

Fig. 24. Spectral time history of received intensities: 8 s, 370 Hz CW transmission, broadside beam; sea-state 4.

intentionally blank page

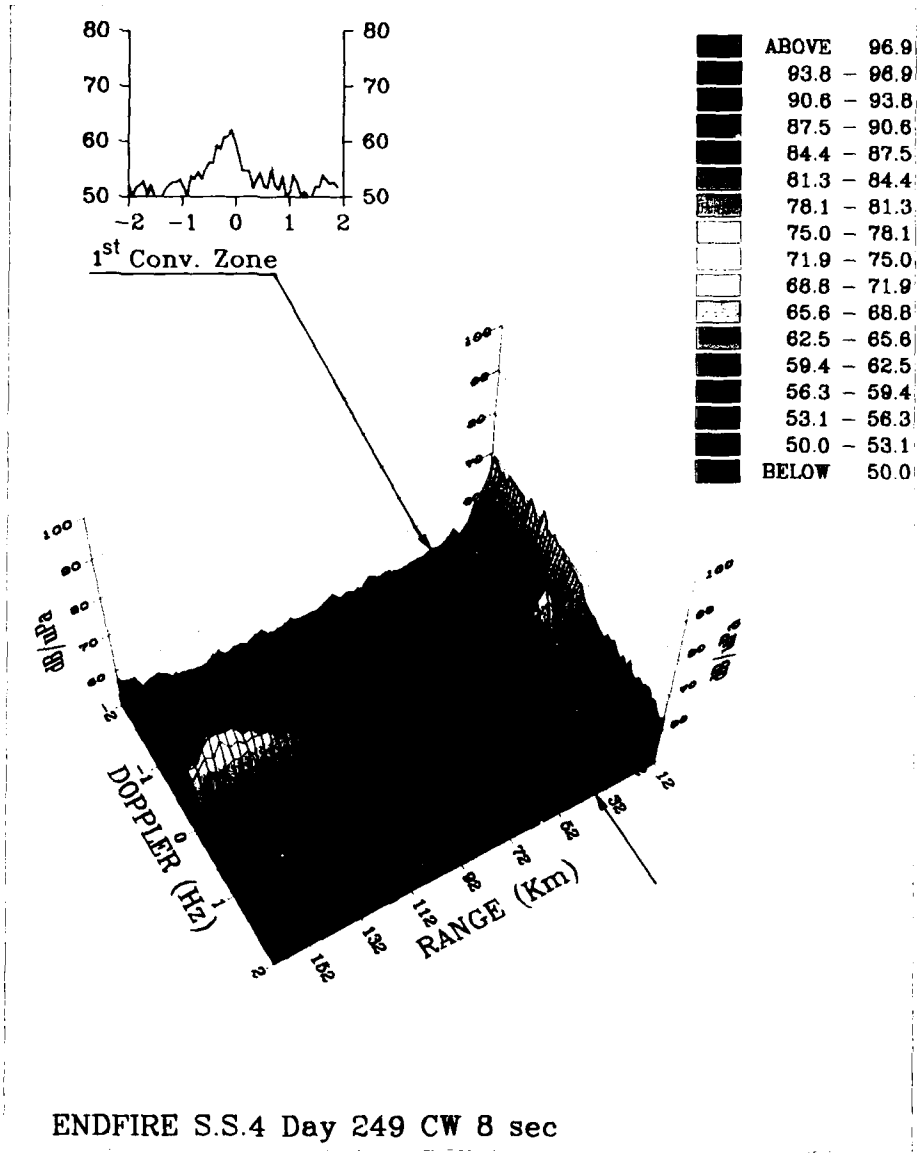

Fig. 25. Spectral time history of received intensities: 8 s, 370 Hz CW transmission; endfire beam; sea-state 4.

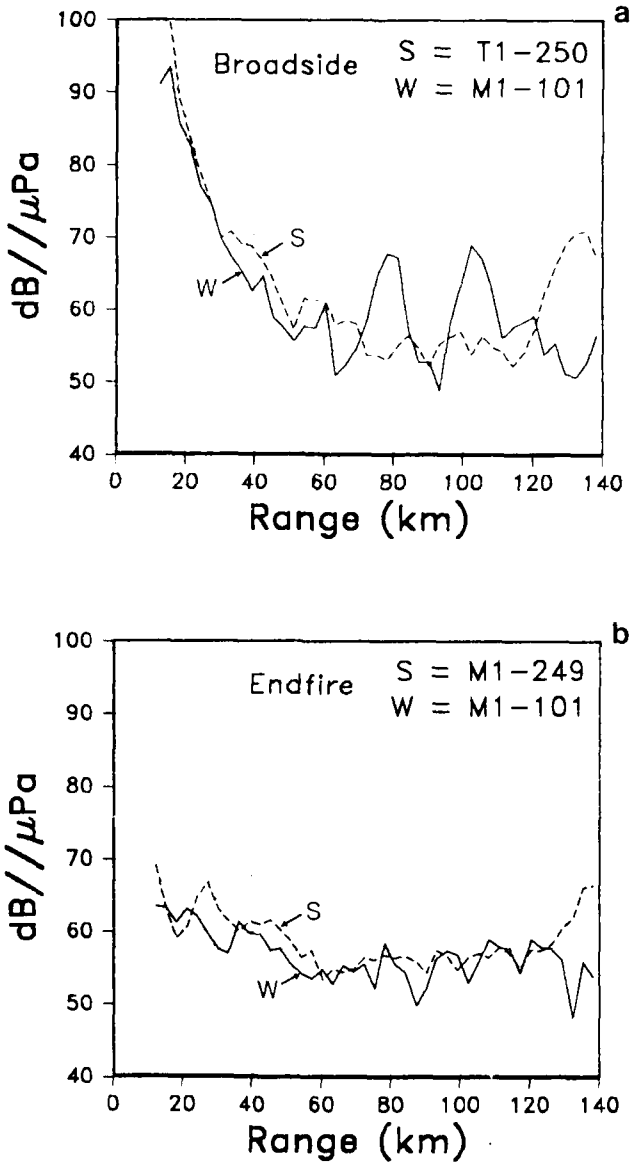

Fig. 26. Comparison of received intensities under winter (curves W) and Summer (curves S) conditions: 8 s, 370 Hz CW pulse, zero-th frequency bin, first 60 km. (a) broadside data; (b) endfire data.

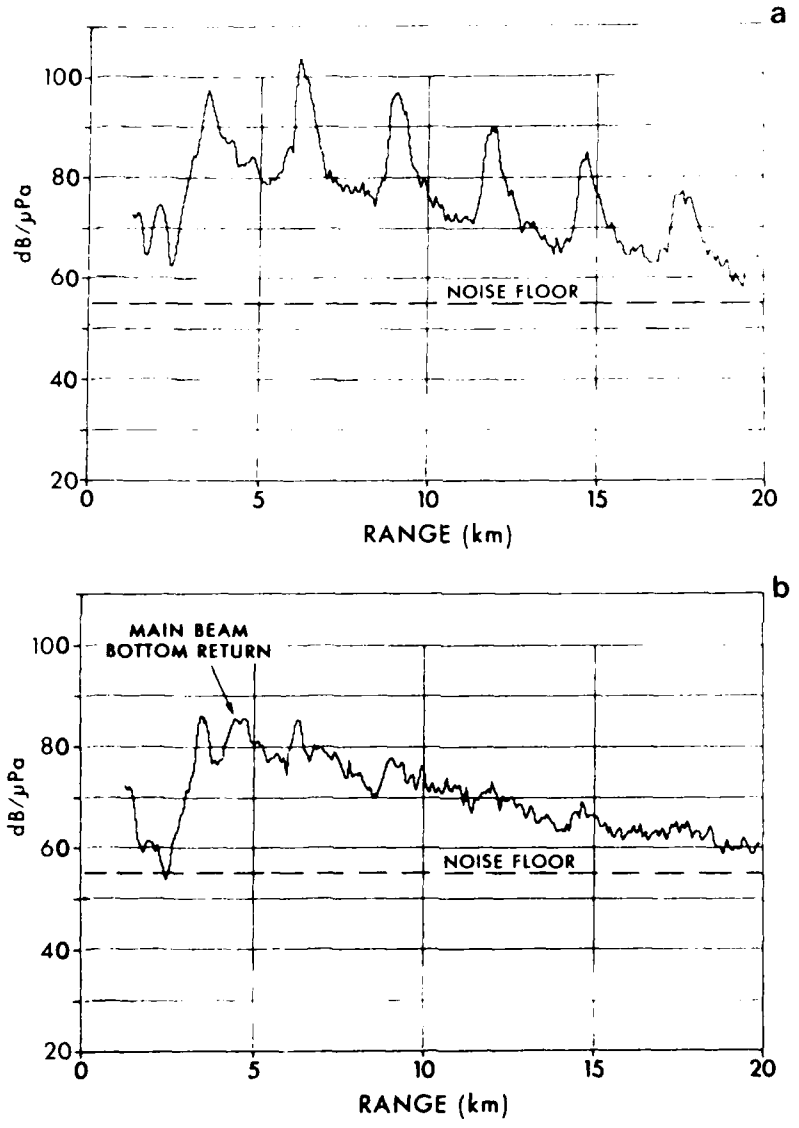

Fig. 27. Reverberation returns over first 20 km: 1 s, 10 Hz linear FM transmission around 370 Hz. (From [26]. (a) broadside beam data; (b) 128° beam (from forward endfire).

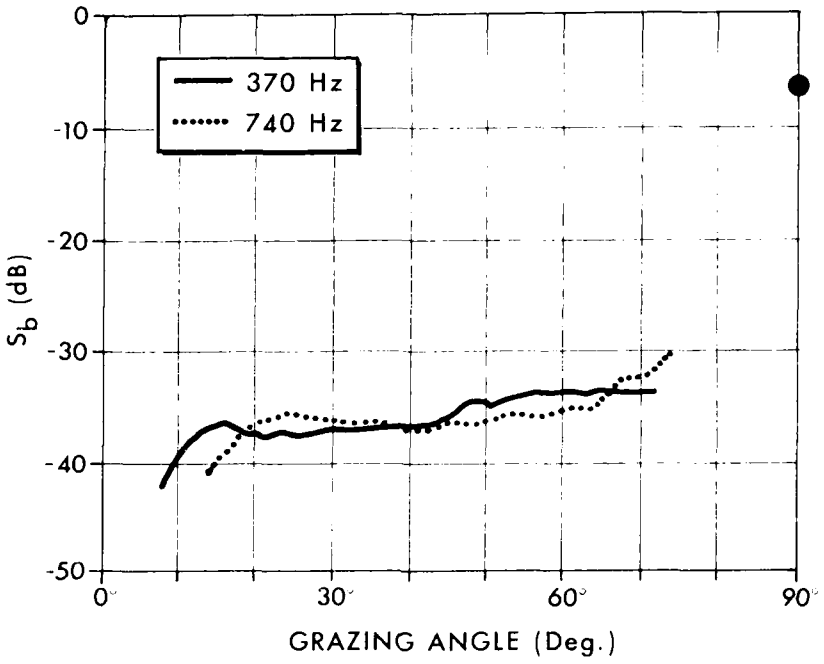

Fig. 28. Typical bottom backscattering strength data vs grazing angle measured in one area of the Balearic Basin. (370 Hz and 740 Hz data).

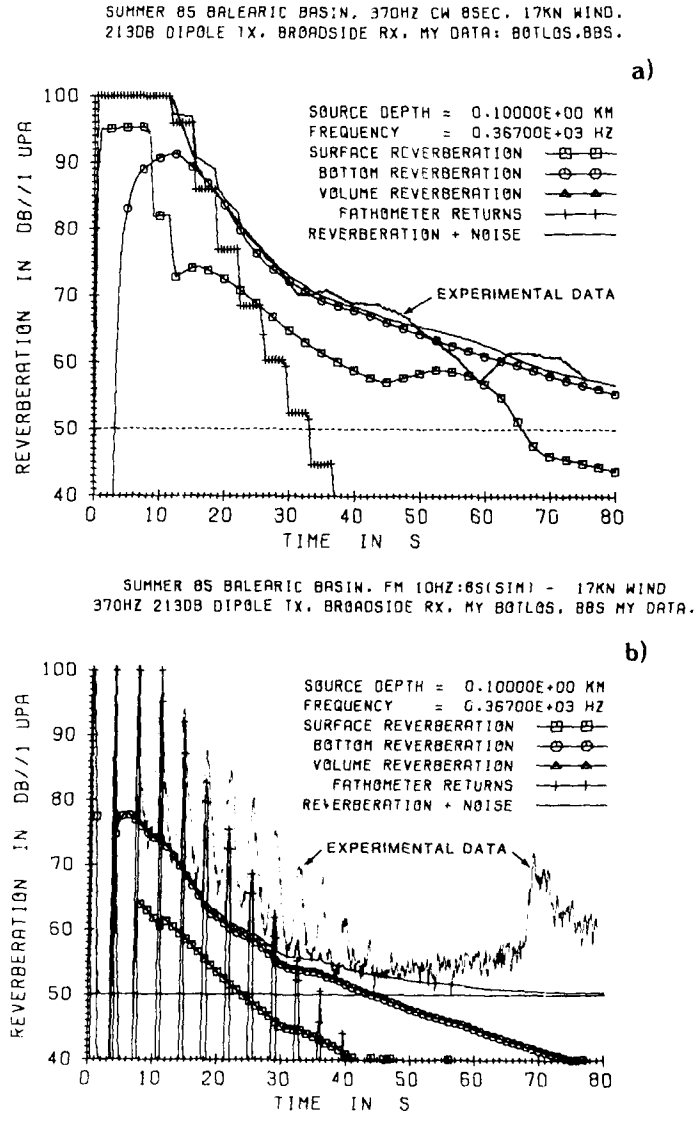

Fig. 29. Comparison of measured reverberation returns vs predictions (with GENERIC Model) over the first 60 km of range; broadside data; summer environment. (a) 8 s, CW pulse (CW data from M1:249); (b) 10-Hz LFM pulse (FM data from M1:249).

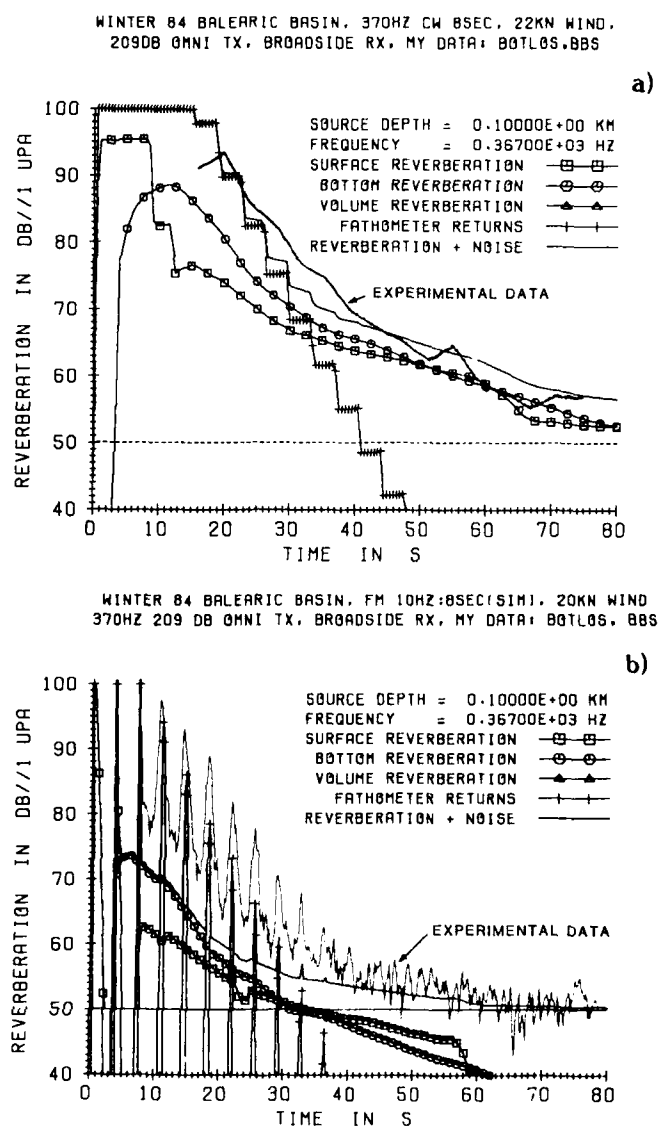

Fig. 30. Comparison of measured reverberation returns vs predictions (with GENERIC Model) over the first 60 km of range: broadside data; winter environment. (a) 8 s, CW pulse (CW data from M1:101); (b) 10-Hz LFM pulse (FM data from M1:101).

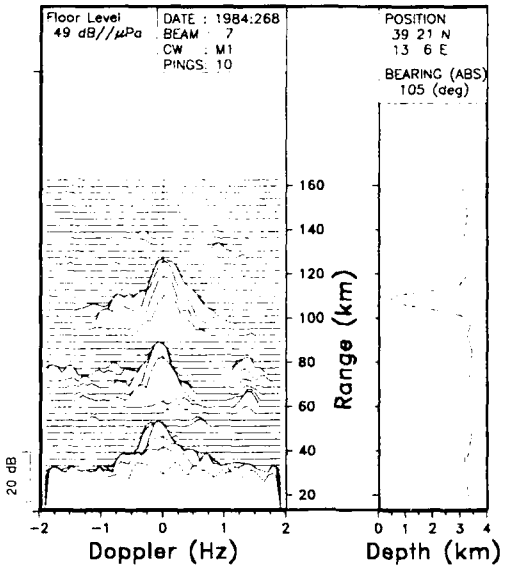

Fig. 31. Spectral time history and bathymetry in selected beam pointing directions (bottom highlight here is Pliny SMT).

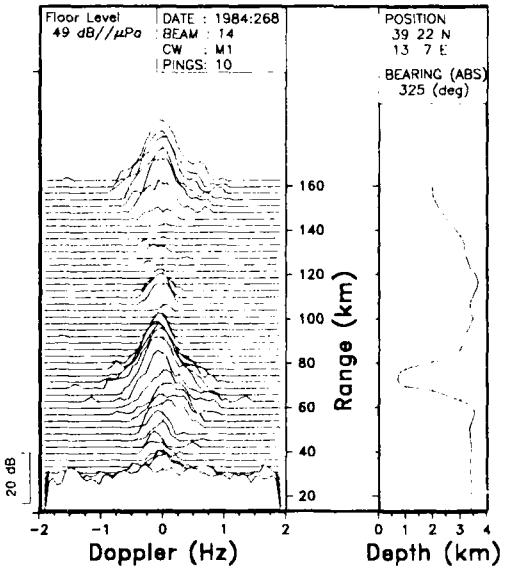

Fig. 32. Spectral time history and bathymetry in selected beam pointing directions (bottom highlight here is Vavilov SMT).

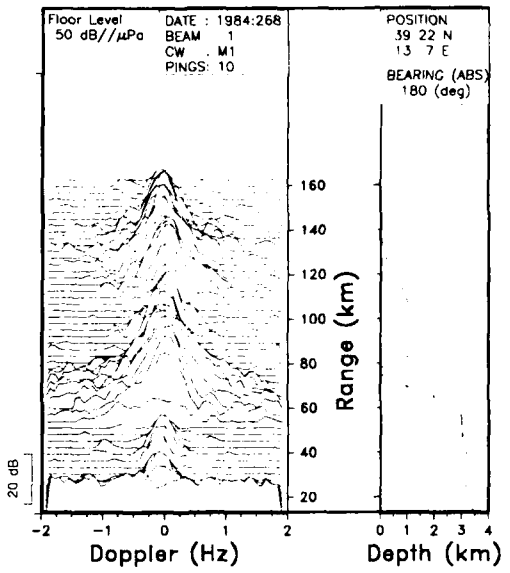

Fig. 33. Spectral time history and bathymetry in selected beam pointing directions (bottom highlight here is Ustica Island).

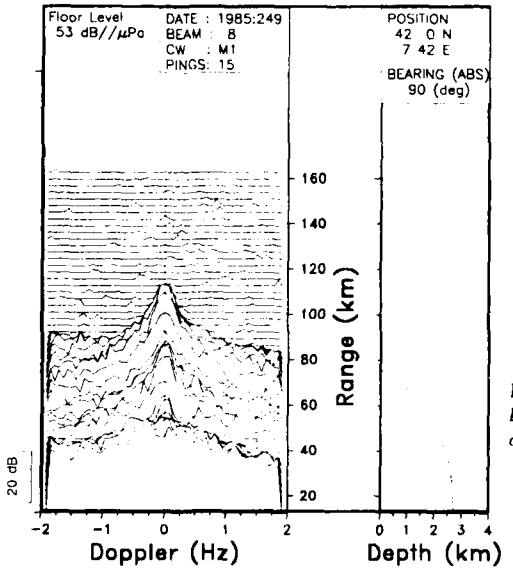

Fig. 34. Spectral time history and bathymetry in selected beam pointing directions (Western coast of Corsica).

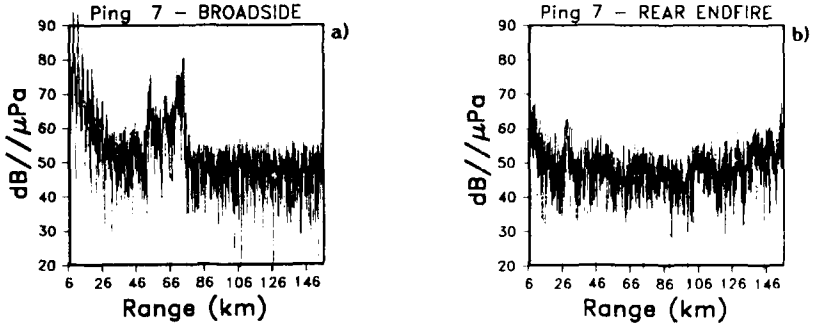

Fig. 35. Single-ping matched-filtered returns over ≃ 160 km; 10 Hz LFM pulse. (a) broadside data; (b) endfire data.

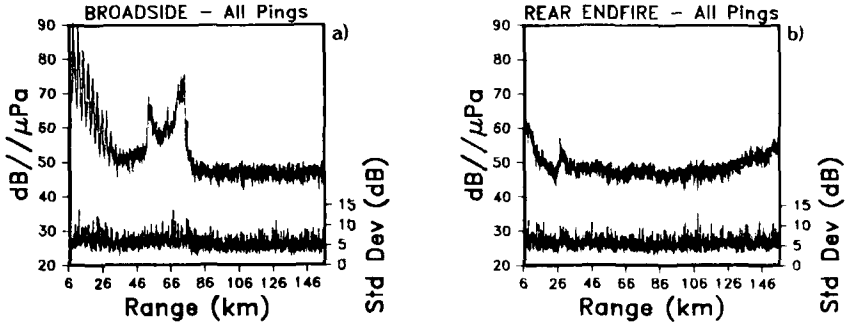

Fig. 36. Ensemble-averaged (17 pings) matched-filtered returns over ≃ 160 km; 10 Hz LFM pulse. Lower curve is dB standard deviation. (a) broadside data; (b) endfire data.

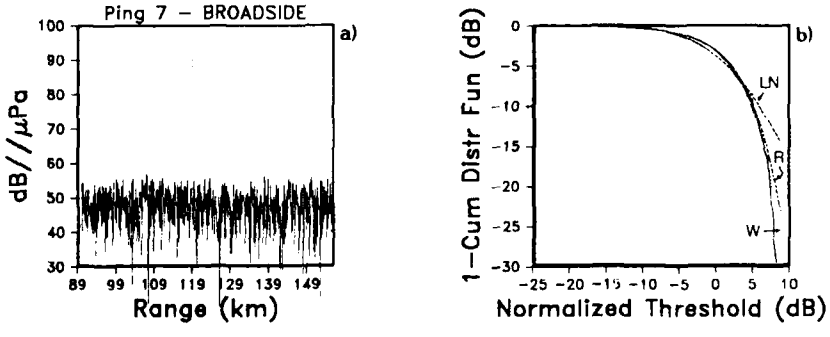

Fig. 37. Comparison of experimental cumulative distribution function vs three theoretical models: Rayleigh (curve R), log-normal (curve LN) and Weibull (curve W). (a) data under test (stationary ambient noise); (b) (1-CDF) vs median-normalized intensities; log/log scale.

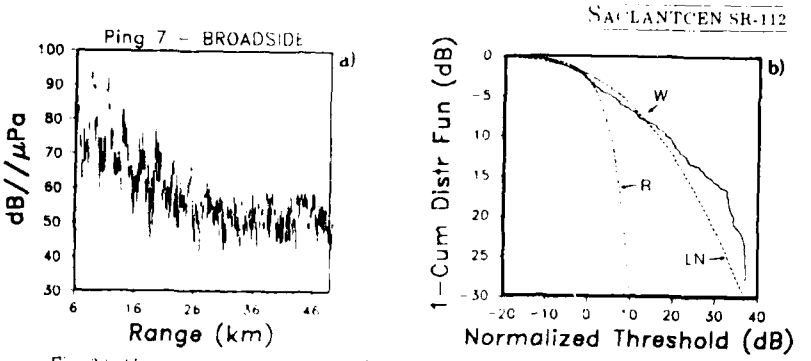

Fig. 38. Comparison of experimental cumulative distribution function vs three theoretical models: Rayleigh (curve R), log normal (curve LN) and Weibull (curve W). (a) data under test (reverberation dominated), (b) (1-CDF) vs median-normalized intensities, log/log scale.

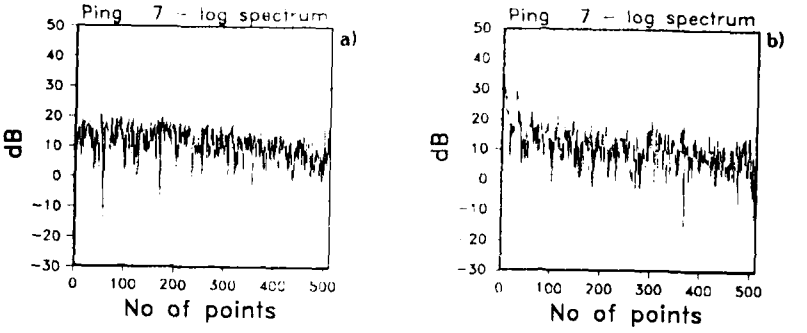

Fig. 39. Power spectra of logarithmic intensities: (a) ambient noise data; (b) reverberation dominated data.

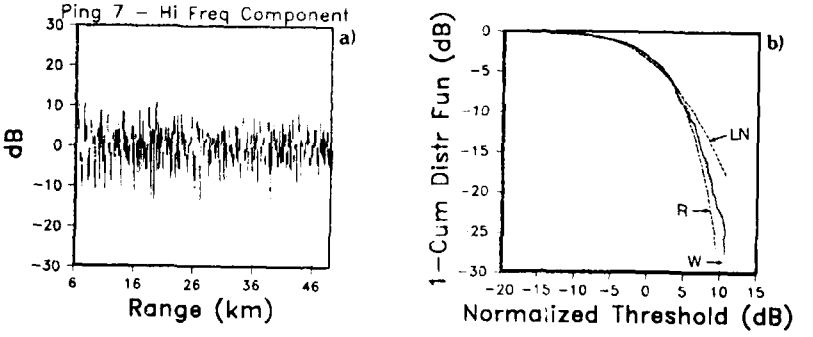

Fig. 40. Comparison of experimental cumulative distribution function vs three theoretical models: Rayleigh (curve R), log-normal (curve LN) and Weibull (curve W). (a) data under test (fluctuations component); (b) (1-CDF) vs median-normalized intensities; log/log scale.

Initial Distribution for SR-112

Ministries of Defence	
JSPHQ Belgium	2
DND Canada	10
CHOD Denmark	8
MOD France	8
MOD Germany	15
MOD Greece	11
MOD Italy	10
MOD Netherlands	12
CHOD Norway	10
MOD Portugal	2
MOD Spain	2
MOD Turkey	5
MOD UK	20
SECDEF US	68
NATO Authorities	
Defence Planning Committee	3
NAMILCOM	2
SACLANT	10
SACLANTREPEUR	1
CINCWESTLANT/ COMOCEANLANT	1
COMSTRIKFLTANT	1
CINCIBERLANT	1
CINCEASTLANT	1
COMSUBACLANT	1
COMMAIREASTLANT	1
SACEUR	2
CINCNORTH	1
CINCSOUTH	1
COMNAVSOUTH	1
COMSTRIKFORSOUTH	1
COMEDCENT	1
COMMARAIRMED	1
CINCHAN	3
SCNR for SACLANTCEN	
SCNR Belgium	1
SCNR Canada	1
SCNR Denmark	1
SCNR Germany	1
SCNR Greece	1
SCNR Italy	1
SCNR Netherlands	1
SCNR Norway	1
SCNR Portugal	1
SCNR Turkey	1
SCNR UK	1
SCNR US	2
SECGEN Rep. SCNR	1
NAMILCOM Rep. SCNR	1
National Liaison Officers	
NLO Canada	1
NLO Denmark	1
NLO Germany	1
NLO Italy	1
NLO UK	1
NLO US	1
NLR to SACLANT	
NLR Belgium	1
NLR Canada	1
NLR Denmark	1
NLR Germany	1
NLR Greece	1
NLR Italy	1
NLR Netherlands	1
NLR Norway	1
NLR Portugal	1
NLR Turkey	1
NLR UK	1
Total external distribution	248
SACLANTCEN Library	10
Stock	22
Total number of copies	280

END

DATE
FILMED

3 88